Tectonics®

RESEARCH ARTICLE
10.1029/2021TC007132

**Key Points:**

- Leech River Shear Zone confirmed as a hot, Eocene-age paleo-subduction interface
- High-temperature metamorphism produced by ridge subduction during accretion of Siletz-Crescent terrane
- New detrital zircon ages from the Leech River Schist support near-trench deposition during Paleocene

**Supporting Information:**

Supporting Information may be found in the online version of this article.

**Correspondence to:**

C. E. Seyler,
caroline.seyler@mail.mcgill.ca

**Citation:**

Seyler, C. E., Kirkpatrick, J. D., Faber, C., Licht, A., Šilerová, D., & Regalla, C. (2022). Structural and metamorphic history of the Leech River Shear Zone, Vancouver Island, British Columbia. *Tectonics*, *41*, e2021TC007132. https://doi.org/10.1029/2021TC007132

Received 2 NOV 2021
Accepted 5 OCT 2022



# Structural and Metamorphic History of the Leech River Shear Zone, Vancouver Island, British Columbia

**C. E. Seyler[1,2], J. D. Kirkpatrick[1], C. Faber[3], A. Licht[4], D. Šilerová[1,5], and C. Regalla[6]**

[1]Department of Earth and Planetary Sciences, McGill University, Montréal, QC, Canada, [2]Now at University of Texas Institute for Geophysics and Department of Geological Sciences, University of Texas, Austin, TX, USA, [3]Department of Geosciences, UiT The Arctic University of Norway, Tromsø, Norway, [4]Aix-Marseille Université, CNRS, IRD, INRAE, Centre de Recherche et d'Enseignement de Géosciences de l'Environnement (CEREGE), Aix-en-Provence, France, [5]Now at Department of Earth Sciences, Simon Fraser University, Burnaby, BC, Canada, [6]School of Earth and Sustainability, Northern Arizona University, Flagstaff, AZ, USA

**Abstract** The Leech River Shear Zone (LRSZ) on southern Vancouver Island separates the metasedimentary schists of the Leech River Complex (LRC) from the accreted oceanic plateau of the Siletz-Crescent terrane. The juxtaposition of these rock units suggests a possible origin as a subduction plate boundary but tectonic context of the LRSZ has yet to be fully established. We present field, microstructural, petrological, and geochronological observations that constrain the structural and metamorphic history of LRSZ. The mylonite zone of the LRSZ straddles the lithologic contact between the schists of the LRC and basalts of the Siletz-Crescent terrane. Foliation orientations, a steeply plunging stretching lineation, and kinematic indicators all suggest reverse-sinistral motion. Compositions of garnet in the schist and amphibole in the metabasalt record synkinematic growth at temperature and pressure conditions of 550°C–570°C and 450–490 MPa. These metamorphic conditions require elevated geotherms that are consistent with plate models that position the Kula-Farallon Ridge and Yellowstone Hotspot in the region in the Eocene (~50 Ma). Detrital zircon U-Pb age distributions for the Leech River Schist have Paleocene maximum depositional ages and are similar to the Upper Nanaimo Group that unconformably overlies the Wrangellia terrane. Our ages support early Paleocene deposition of the schist in a subduction trench/slope environment followed by underthrusting and underplating. These results establish the exhumed mylonite zone of the LRSZ as a paleo-plate interface that was active during Eocene subduction.

## 1. Introduction

Subduction zone dynamics are strongly influenced by the mechanical properties of subduction interface shear zones (Behr et al., 2022). However, the relevant properties of subduction interfaces, such as their widths, rock types, and internal structure, cannot be determined via geophysical observation. Instead, field- and microscale observations of exhumed shear zones that were active during subduction are needed to fill this knowledge gap. Subduction dynamics and thermal gradients evolve as they mature (e.g., Holt & Condit, 2021), and subduction zones can encompass a broad range of environments (Chelle-Michou et al., 2022), for example, when influenced by atypical subduction geometries like ridge subduction (e.g., Brown, 1998; DeLong et al., 1979; Sakaguchi, 1996). A more complete inventory capturing the variability of subduction interfaces is therefore needed to better understand their behavior.

The Canadian Cordillera potentially exposes numerous subduction-related structures as it was assembled through a series of accretionary orogenies. One candidate structure is the Leech River Fault (Figure 1), a terrane-bounding fault located on southern Vancouver Island in British Columbia that juxtaposes mafic volcanic and igneous rocks of the Metchosin Igneous Complex (MIC) to the south with the predominantly metapelitic Leech River Complex (LRC). For clarity, we will term this structure the "Leech River Shear Zone" (LRSZ) to differentiate it from the recently active "Leech River Fault," which is locally coincident (Harrichhausen et al., 2021; Li et al., 2018; Morrell et al., 2017, 2018). The MIC is part of the Siletz-Crescent terrane, a ~10- to 30-km-thick sequence of Eocene mafic volcanics and intrusive suites that extends from Vancouver Island to Oregon. Trace element and rare earth element geochemistry of basalts from the terrane (Phillips et al., 2017), combined with the terrane's thickness (Clowes et al., 1987; Tréhu et al., 1994), indicate the Siletz-Crescent terrane represents a portion of a large igneous province that formed on the Farallon plate, near the Kula/Resurrection-Farallon ridge, and above

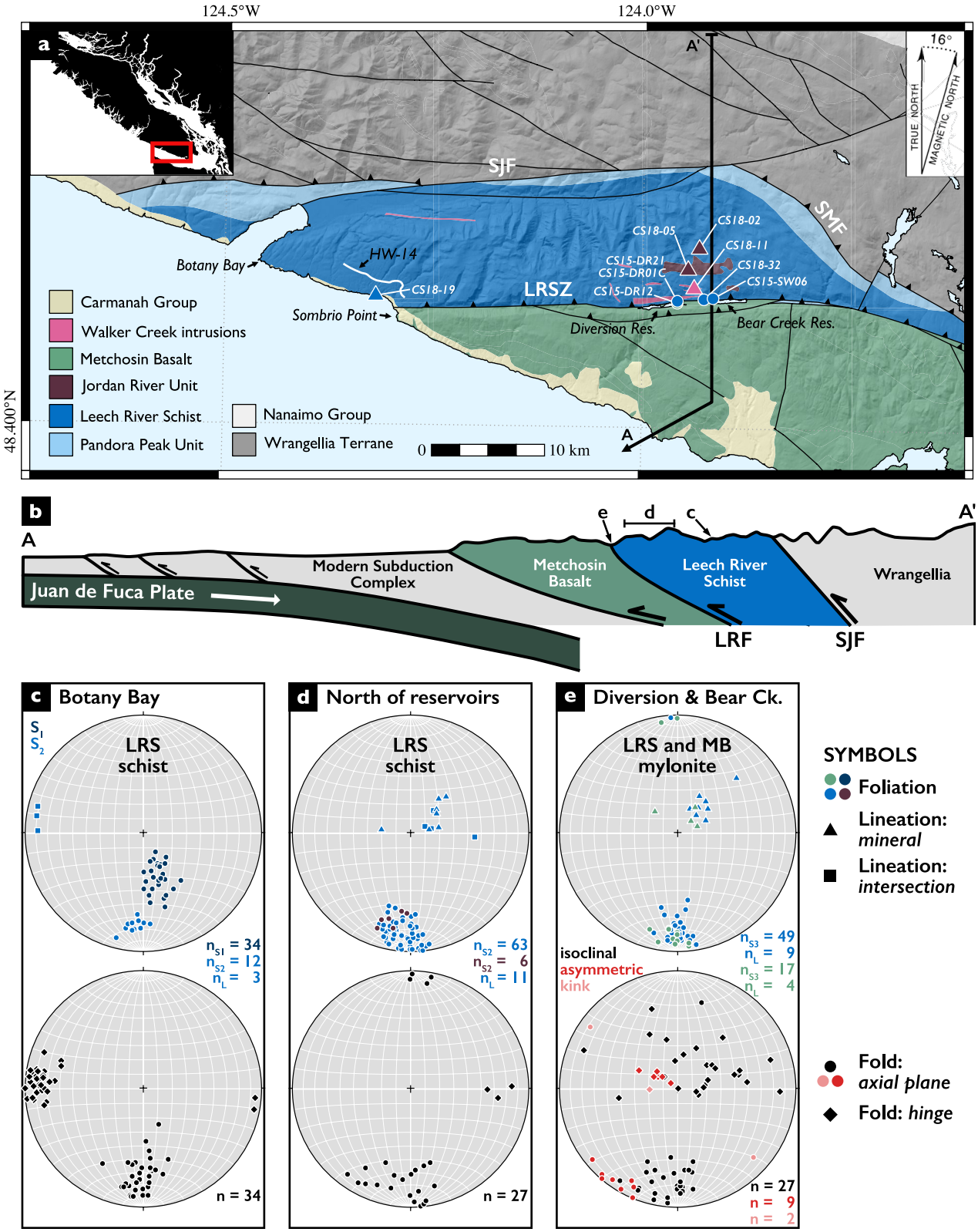


**Figure 1.**

a mantle plume, potentially the Yellowstone Hotspot (Phillips et al., 2017; Wells et al., 2014). Accretion of the Siletz-Crescent terrane is therefore inferred to have occurred during subduction and impacted the deformation of the subduction forearc and tectonics of the upper plate (Eddy et al., 2016).

Previous work on the LRSZ presents conflicting interpretations of the tectonic context of this structure. Seismic reflection images show the contact between the LRC and MIC extends from the surface trace of the LRSZ and dips to the north under Vancouver Island and projects to the surface trace of the LRSZ (Clowes et al., 1987; Matharu et al., 2014). Combined with the ages of the LRC (Cretaceous; Groome et al., 2003) and MIC (Eocene; Duncan, 1982; McCrory & Wilson, 2013), this geometry suggests the LRSZ hosted reverse-sense motion, consistent with formation in a subduction setting. However, previous field data suggest dominantly strike-slip motion (Fairchild & Cowan, 1982; Groome, 2000), possibly related to development of a forearc rift basin formed on the continental margin, which was previously proposed as the tectonic origin of the MIC (Babcock et al., 1992; Wells et al., 1984). The origin of the LRC is also uncertain due to the lack of a depositional age and its previous interpretation as allochthonous to Vancouver Island (Fairchild & Cowan, 1982).

In this study, we use structural, petrological, and geochronological data to reevaluate the tectonic origin of the LRSZ and the LRC. We directly tested the thrust versus strike-slip faulting regime with field and microstructural observations that establish the kinematics of deformation. We probed mineral compositions (garnet and amphibole), applied the Ti-in-biotite geothermometer, and conducted phase equilibrium modeling to develop metamorphic histories for the shear zone rocks and determine the synkinematic *P-T* conditions. We also measured the U-Pb dates of detrital zircons from the LRC to determine its depositional age and setting. Our results provide the first constraints on the paleogeographic and tectonic origin of the LRC and the synkinematic pressure, temperature, and timing of deformation on the LRSZ. The results indicate that the LRSZ was an Eocene-age, hot subduction interface that formed during underthrusting of the Siletz-Crescent terrane beneath the previously underplated LRC as the Farallon plate subducted under North America.

## 2. Geologic Setting

The LRSZ is an east-west trending, terrane-bounding structure that separates the LRC north of the fault from the MIC to the south. The LRC, together with the Pandora Peak Unit and Pacific Rim Complex, collectively make up the Pacific Rim terrane, a southern correlative of the Chugach-Prince William accretionary complexes in Alaska (Cowan, 2003; Cowan et al., 1997; Garver & Davidson, 2015). The MIC, the Crescent Formation of Washington, the Coast Range Volcanic Province of Washington and Oregon, and the Siletz River Volcanics of Oregon comprise the Siletz-Crescent terrane (Duncan, 1982; Irving, 1979; McCrory & Wilson, 2013; Simpson & Cox, 1977).

### 2.1. Leech River Shear Zone

The LRSZ has been previously reported as a fault zone with two to four discrete left-lateral strike slip faults, lacking any fault gouge, breccia, or mylonitization (Fairchild & Cowan, 1982) as well as a left-lateral shear zone composed of mylonites ("Bear Creek Shear Zone" in Groome (2000)). The interpretation of the LRSZ as a left-lateral strike slip fault was largely based on the regional steep dip of the fault (Fairchild & Cowan, 1982). Limited observations of shear sense indicators from mylonites within the Bear Creek Shear Zone indicate left-lateral motion (Groome, 2000). Quaternary reactivation of this structure as a wide zone of strike-slip faults has been documented through identification of fault scarps (Morell et al., 2017), microseismicity (Li et al., 2018), and paleoseismic trenching (Harrichhausen et al., 2021; Morell et al., 2018). Here, we focus on the ancient structure that established the tectonic contact between the LRC and MIC (the "Leech River Shear Zone"), rather than

**Figure 1.** Geologic map, cross section, and structural data. (a) Simplified geologic map of southern Vancouver Island (adapted from Cui et al. (2017), Groome et al. (2003), Muller (1980), and Rusmore (1982)). Locations labeled with black arrows indicate field sites. Circles and triangles represent locations of samples collected for petrography and U-Pb zircon geochronology, respectively, with colors corresponding to the sampled units. LRSZ—Leech River Shear Zone; SJF—San Juan Fault; and SMF—Survey Mountain Fault. (b) Simplified geologic cross section (adapted from Clowes et al. (1987) and Hyndman et al. (1990)). Stereonet projections of foliation, lineation, and fold orientations. (c) Foliation, lineation, and fold orientations in the Leech River Schist (LRS) near Botany Bay (~0.5 $km^2$ area). (d) Foliation, lineation, and fold orientations within the LRS directly north of the Diversion and Bear Creek reservoirs (up to ~2 km north of the LRSZ). (e) Foliation, lineation, and three sets of fold orientations within the LRS and Metchosin Basalt mylonites (~12 km along strike within the shear zone). Note that isoclinal folds with shallowly plunging hinges are underrepresented due to lack of subvertical exposures. Foliation planes and fold axial planes are plotted as poles to the planes. Structural field data can be obtained in Table S2.

the recently active "Leech River Fault," which is locally parallel and colocated with the terrane boundary and mylonite zone of the LRSZ.

### 2.2. Leech River Complex

The LRC is an approximately 10-km-thick package of metasedimentary rocks that crop out in an east-west trending unit on southern Vancouver Island (Figure 1). The LRC is bounded to the north by the San Juan and Survey Mountain faults, which juxtapose the LRC with the Wrangellia terrane and the Pandora Peak Unit of the Pacific Rim terrane, respectively (Rusmore & Cowan, 1985). The LRC includes the Leech River Schist (LRS), the Jordan River Unit, the Tripp Creek Metabasite, and the Walker Creek intrusions (Fairchild & Cowan, 1982).

The LRS is a metapelitic schist containing metapsammitic layers. Based on the assemblage of discontinuous layers of metamorphosed shales and sandstones with minor chert and basaltic volcanics, the LRS was interpreted as a submarine, near-continental margin turbidite sequence deposited near a source of basalt, such as a spreading ridge (Fairchild & Cowan, 1982; Muller, 1977b, 1980). The LRS has a reported maximum depositional age (MDA) of 103 Ma derived from the youngest detrital zircon dated by Groome et al. (2003). Fairchild and Cowan (1982) reported transposed sedimentary layering, aligned metapsammitic lenses within a metapelitic matrix, and two generations of folds with strong axial planar foliation parallel to the compositional layering. These features were interpreted to result from regional north-south shortening (Fairchild & Cowan, 1982). The metamorphic grade of the LRS increases from greenschist facies in the north (chlorite-white mica-biotite phyllites) to amphibolite facies in the south (garnet-staurolite-andalusite schists), and metamorphism was syn- to postkinematic with regional deformation (Fairchild & Cowan, 1982; Groome et al., 2003; Rusmore & Cowan, 1985). Previous work indicated that the metamorphic gradient was isobaric based on the progression of metamorphic assemblages through a series of east-west isograds for biotite, garnet, staurolite, and andalusite (Rusmore & Cowan, 1985). Estimates of peak pressure (<350 MPa) and temperature (500°C–600°C) are attributed to the presence of andalusite in the southern region within contact aureoles around intrusive units (Groome et al., 2003; Rusmore, 1982).

The Jordan River Unit is a quartz-feldspar-biotite schist that has been interpreted as both the largest body of metasandstone in the LRS (i.e., the Valentine metasandstone in Fairchild and Cowan (1982); Muller (1980)) and as a plagioclase-rich peraluminous metagranodiorite intrusion derived from anatexis of the LRS with a titanite U-Pb crystallization age of 88 Ma (Groome et al., 2003). The Tripp Creek Metabasite is an actinolite-plagioclase-quartz-garnet schist interpreted as an intrusive unit due to the presence of foliated LRS xenoliths (Groome et al., 2003). The Jordan River Unit and Tripp Creek Metabasite have a schistosity parallel to the foliation in the LRS, suggesting their formation is pre- to synkinematic with deformation of the complex. The Walker Creek intrusions are a suite of tonalite, trondhjemite, and granodiorite dikes and sills present in the southern portion of the LRS. Deformation of these intrusions is nonuniform, with some dikes displaying schistosity parallel to the foliation in the LRS while others remain undeformed, suggesting syn- to postkinematic magmatism (Groome et al., 2003). These intrusions have zircon U-Pb crystallization ages ranging from 51 to 47 Ma, and their geochemical signatures suggest they are derived from anatexis of the LRS (Groome et al., 2003).

### 2.3. Metchosin Igneous Complex

The MIC consists of a 3-km-thick ophiolitic pseudostratigraphy consisting of gabbro stocks (Sooke Gabbros), sheeted dikes, and a sequence of basalt flows that transitions from submarine to subaerial up-section (Massey, 1986). Whole rock trace element geochemistry is transitional between N-MORB and E-MORB signatures, suggesting both spreading ridge- and mantle plume-related magmatism (Duncan, 1982; Phillips et al., 2017; Timpa et al., 2005). The age of the complex ranges from 58 to 52 Ma based on $^{40}Ar/^{39}Ar$ fusion dates and U-Pb zircon dates (Duncan, 1982; Massey, 1986; Yorath et al., 1999). Temperature estimates from amphibole compositions and $Al^{iv}$-in-chlorite geothermometry suggest the metamorphic grade in the complex increases from prehnite-actinolite in the east to amphibolite in the west along a ~5°C to 10°C/km horizontal gradient (Timpa et al., 2005). This gradient was interpreted as the result of metamorphism during tectonic emplacement of the MIC followed by differential exhumation (Timpa et al., 2005).

Two contrasting origins for the Siletz-Crescent terrane have been proposed: An oceanic plateau (originally proposed by Duncan (1982)) or extensional volcanism in a forearc rift (Babcock et al., 1992; Wells et al., 1984). However, the revised 55–49 Ma age range for the terrane (Eddy et al., 2017; McCrory & Wilson, 2013; Wells

et al., 2014 and references therein), plate reconstruction modeling (McCrory & Wilson, 2013; Wells et al., 2014) and basalt geochemistry (Phillips et al., 2017) suggest that the Siletz-Crescent terrane represents an accreted oceanic plateau that formed near the Kula/Resurrection-Farallon Ridge by a near-ridge mantle plume, most likely the Yellowstone Hotspot (Duncan, 1982; Eddy et al., 2016, 2017; McCrory & Wilson, 2013; Phillips et al., 2017; Wells et al., 2014). Shortly after its formation, the Washington and Oregon portion of the terrane docked to North America by 51–48 Ma based on the coccolithophores present in the overlying strata (Wells et al., 2014), the sedimentary record of changing paleoflow direction (Eddy et al., 2016), and the age of intrusives (Eddy et al., 2017). On Vancouver Island, the terrane docked prior to 45–42.5 Ma based on $^{40}Ar/^{39}Ar$ cooling ages in mica that record exhumation of the LRS (Groome et al., 2003), which is inferred to have been due to uplift related to MIC underplating.

## 3. Methods

### 3.1. Detrital Zircon Analysis

Detrital zircon ages were determined for samples of the LRS, Jordan River Unit, and Walker Creek intrusions (sample locations in Table S1 in Supporting Information S1). Detailed data acquisition and reduction protocols are described in Shekut and Licht (2020). Zircons were extracted by heavy mineral separation, including concentration with a Holman-Wilfley™ gravity table, density separation with methylene iodide, and magnetic separation with a Frantz™ Magnetic Barrier separator. Data were collected using a laser-ablation inductively coupled-plasma mass-spectrometry (LA-ICP-MS), using an iCAP-RQ Quadrupole ICP-MS coupled to an Analyte G2 excimer laser at the University of Washington, using a spot diameter of 25 microns and Plešovice zircons as calibration reference material (Sláma et al., 2008). Data reduction was conducted with *Iolite* (Version 3.5), using their *U_Pb_Geochron4* Data Reduction Scheme to calculate U-Pb dates uncorrected for common lead (Paton et al., 2010). Uncertainties for all samples were calculated using a modified version of the method of Matthews and Guest (2017) that takes into account the impact of $^{207}Pb$ beam intensity on date uncertainties (Horstwood et al., 2016). The dates used for plotting are $^{206}Pb/^{238}U$ for dates <1,400 Ma and $^{207}Pb/^{206}Pb$ for dates >1,400 Ma. Dates >300 Ma were screened for concordance using a discordance filter at >20% discordance (<80% concordance) and >5% reverse discordance (>105% concordance); we used the $^{206}Pb/^{238}U$ versus $^{207}Pb/^{235}U$ ratio to calculate discordance for dates <1,300 Ma, and the $^{206}Pb/^{238}U$ versus $^{207}Pb/^{206}Pb$ ratio for older dates. A subset of zircon grains from each sample were imaged using cathodoluminescence to assess their growth textures (Figure S1 in Supporting Information S1). MDAs were calculated from the youngest age population of overlapping dates ($n \geq 3$) using the *TuffZirc* application within IsoPlot (Ludwig, 2003).

### 3.2. Mineral Composition Analysis

Electron probe microanalysis was conducted on representative thin sections of the schist and metabasalt mylonites from the LRSZ to determine the synkinematic *P-T* conditions. Polished thin sections were prepared perpendicular to the foliation and parallel or perpendicular to the lineation from oriented samples (Table S1 in Supporting Information S1). Mineral compositions were measured with five wavelength-dispersive spectrometers on either a JEOL 8900 electron microprobe or Cameca SX100 Five-FE electron microprobe. Garnet compositions were measured on a Cameca microprobe with an accelerating voltage of 15 kV, a beam current of 20 nA, and a beam diameter of 5 μm. Biotite compositions from samples CS15-DR21 and CS15-SW06 were measured on a JEOL microprobe with an accelerating voltage of 15 kV, a beam current of 20 nA, and a beam diameter =10 μm. Biotite from samples CS18-25 and CS18-32 were measured on a Cameca microprobe with an accelerating voltage of 15 kV, a beam current of 20 nA, and a beam diameter of 5 μm. Amphibole compositions were measured on a Cameca microprobe with an accelerating voltage of 20 kV, a beam current of 4 nA, and a beam diameter of 5 μm. Amphibole compositions were calculated based on the recommendations and classification scheme approved by the Commission on New Minerals Nomenclature and Classification of the International Mineralogical Association (Hawthorne et al., 2012; Locock, 2014). Plagioclase compositions were measured on a Cameca microprobe with an accelerating voltage of 15 kV, a beam current of 20 nA, and a beam diameter of 5 μm. Bulk rock compositions were determined by Actlabs using whole rock fusion X-ray fluorescence analysis. Phase equilibrium modeling was conducted with *PerpleX* software (version 6.9.9; Connolly, 2005) using the internally consistent data set of Holland and Powell (1998, revised 2004).

## 4. Field Observations of the Hanging Wall and Footwall

In this section, we describe the LRS to the north and MIC to the south to differentiate the deformation associated with the shear zone from regional structures. Our study area extends from the western coast of the island to the Diversion and Bear Creek reservoirs (Figure 1). Exposures are best along the coast, in road cuts along Highway 14 and logging roads north of the reservoirs, and around the shores of the reservoirs. Elsewhere, the exposure is very poor due to dense vegetation and till cover. Targeted field sites include Botany Bay (LRS), north of the reservoirs (LRS), and Sombrio Point (Metchosin Basalt).

### 4.1. Leech River Schist (Hanging Wall of the LRSZ)

The structural fabrics and metamorphic grade of the LRS vary throughout the unit. We describe the schist in two localities to illustrate this variability: A ~0.5 km$^2$ area around Botany Bay located ~5 km north of the mapped trace of the LRSZ (projected offshore) and north of the Diversion and Bear Creek reservoirs, a transect from the northern edge of the high strain zone up to ~2 km north of the LRSZ.

At Botany Bay, the schist is characterized by a block-in-matrix fabric with quartz- and plagioclase-rich metapsammitic blocks hosted in a phyllosilicate-rich metapelitic matrix (Figures 2a–2d). Some larger blocks contain evidence for graded bedding and crossbeds indicating that the lithologic variation represents primary sedimentary bedding ($S_0$), which included interbedded sand-, silt-, and clay-sized layers. The present-day layer discontinuity and strong deformation fabrics in the matrix, including solution cleavage, imply that bedding was tectonically disrupted and transposed into the block-in-matrix fabric. Block sizes range from centimeter- to meter-scale and larger blocks commonly contain quartz veins that terminate at the block edges. Two foliation orientations are present, with the dominant foliation ($S_1$) defined by parallel long axes of blocks forming an apparent layering that is parallel to a continuous cleavage in the metapelitic matrix. A less pronounced, spaced cleavage ($S_2$) in the metapelitic matrix is discordant to the $S_1$ cleavage (Figure 2a). Both $S_1$ and $S_2$ strike approximately east-west, but $S_2$ is more steeply dipping, resulting in an intersection lineation that plunges shallowly to the west (Figures 1c and 3a). Some quartz veins within the blocks are tightly folded with axial surfaces parallel to the $S_1$ foliation. Asymmetric isoclinal folds of thin metapsammitic blocks intrafolial with $S_1$ are also observed, which indicate that $S_0$ is transposed into $S_1$ (Figure 2b). The $S_2$ foliation is axial planar to tight, asymmetric, and disharmonic folding of the $S_1$ foliation, which exhibits a top-to-the-south vergence direction (Figure 2c). Later quartz veins crosscut both the blocks and matrix at a low angle to $S_1$ foliation and are moderately deformed into the $S_1$ foliation (Figure 2d). The $S_2$ foliation is defined by white mica and chlorite, indicating deformation at greenschist conditions (Rusmore, 1982).

North of the Diversion and Bear Creek reservoirs, the schist is characterized by disordered and discontinuous deformation fabrics rather than a block-in-matrix structure (Figure 2e). The dominant foliation is defined by dismembered compositional layering of metapsammitic and metapelitic layers (millimeters to 2- to 3-cm thick), which is transposed and locally parallel to a grain shape preferred orientation of phyllosilicate minerals in the phyllitic layers. The compositional layering is transposed, with an axial planar cleavage. This composite foliation is wavy and irregular, strikes roughly east-west, and dips steeply to the north (Figure 1d). Asymmetric, tight folds of the layering with parasitic folding are common in both subhorizontal and subvertical sections with top-to-the-west and top-to-the-south vergence, respectively. The similar attitudes of the dominant foliation in this region to the $S_2$ foliation near Botany Bay, along with the similar vergence direction of asymmetric folds, suggests foliations formed under the same shortening direction. We interpret the dominant foliation north of the reservoirs as an $S_2$ foliation that has transposed and folded the $S_0$–$S_1$ foliation (cf. Fairchild & Cowan, 1982). Quartz veins crosscut the foliation at low and high angles and are often boudinaged and folded with the foliation. Coarse-grained (~1 to 10 mm) metamorphic minerals of garnet, biotite, staurolite, and andalusite are sometimes present in outcrop, indicating amphibolite grade metamorphism. The foliation is deflected around these grains, suggesting porphyroblast growth was pre- and/or synkinematic. Overall, the highly dismembered compositional layers, smaller scale of quartz-plagioclase boudins, and transposition of the $S_1$ foliation to parallel with $S_2$ suggest that this region is relatively higher strain compared to the schist at Botany Bay.

#### 4.1.1. Detrital Zircon U-Pb

We investigated the origin of the LRC with detrital zircon geochronology to reevaluate its depositional age and help determine if the Jordan River Unit is metasedimentary or intrusive. U-Pb ages were analyzed from zircon

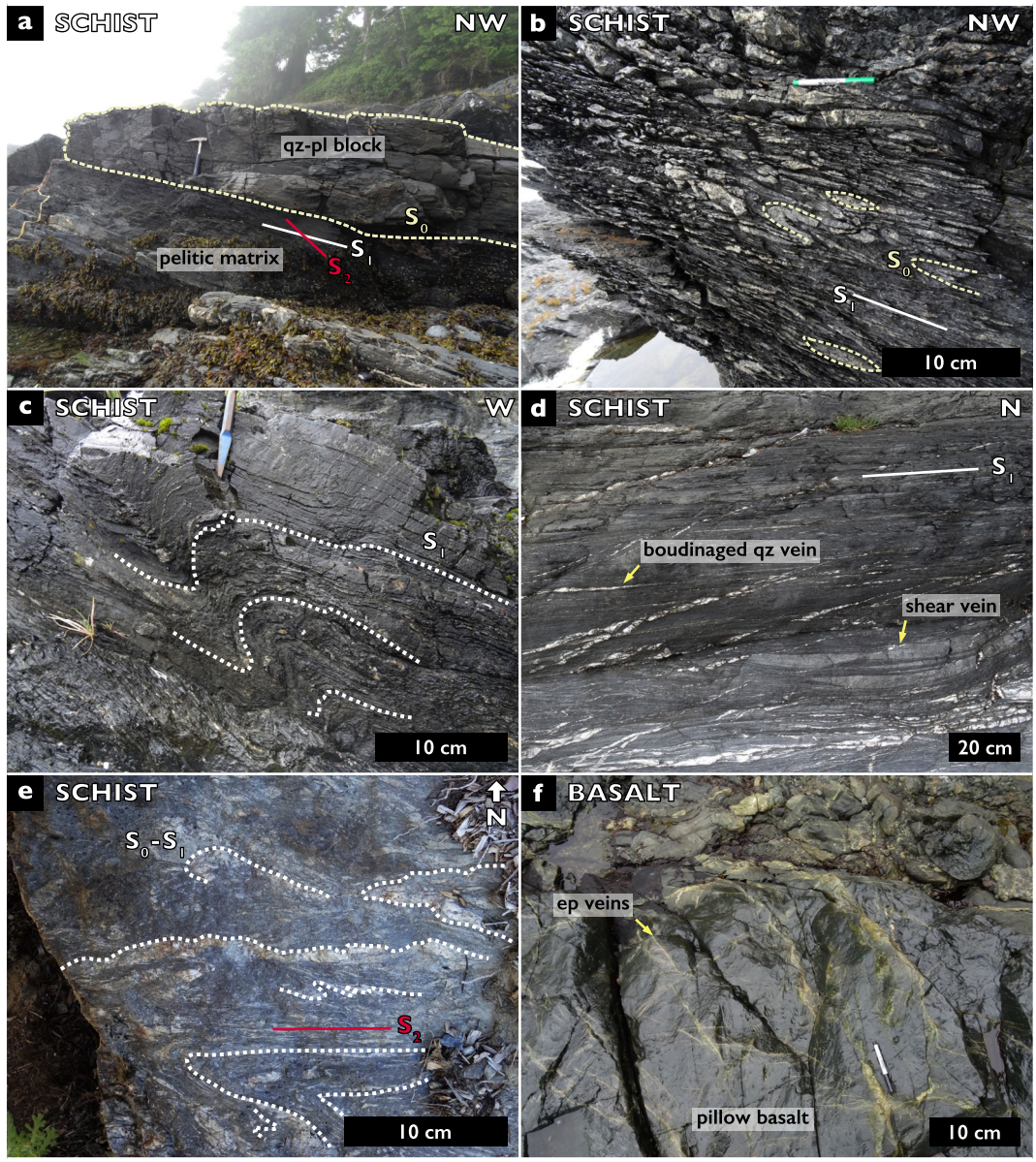


**Figure 2.** Field photos of structures in the hanging wall and footwall. Photos are from Botany Bay (a)–(d), north of the Diversion and Bear Creek reservoirs (e), and Sombrio Point (f). (a) Leech River Schist (LRS) at Botany Bay contains centimeter- to meter-scale quartz-plagioclase blocks within a phyllosilicate-rich matrix, which defines a block-in-matrix texture and preserves original bedding ($S_0$) between sandstone layers and shale. The matrix has two foliation orientations ($S_1$ and $S_2$), with $S_1$ subparallel to the long axes of blocks. (b) Isoclinal folding of the $S_{0-1}$ foliation with subparallel axial planes. (c) Asymmetric, disharmonic folding of the $S_1$ foliation with axial planes subparallel to the $S_2$ foliation. (d) Quartz veins within the LRS are oriented 0°–30° from the $S_1$ foliation. Some shear veins host small amounts of displacement, while the veins subparallel to foliation are offset along $S_1$. (e) LRS directly north of the Diversion and Bear Creek reservoirs is composed of discontinuous quartz-plagioclase layers and micaceous layers. The $S_0$–$S_1$ foliation is transposed into parallel with the dominant $S_2$ foliation and tightly folded into disharmonic and often asymmetric folds. (f) Metchosin Basalt at Sombrio Point contains pillow basalts with abundant epidote veins.

grains in four samples (sample locations in Figure 1a): One sample of Walker Creek intrusions, one sample of LRS, and two samples of the Jordan River Unit, which has been inconsistently described as either a metasandstone (Fairchild & Cowan, 1982; Muller, 1980) or an igneous intrusion (Groome et al., 2003).

The MDA of the LRS sample is 64.4 ± 2.4 (2$\sigma$) Ma and the MDA of the Jordan River samples are 66.9 ± 2.1 and 61.0 ± 2.3 Ma (2$\sigma$) (Figure 3a, Table S3). Zircons in the LRS and Jordan River metasandstone are detrital,

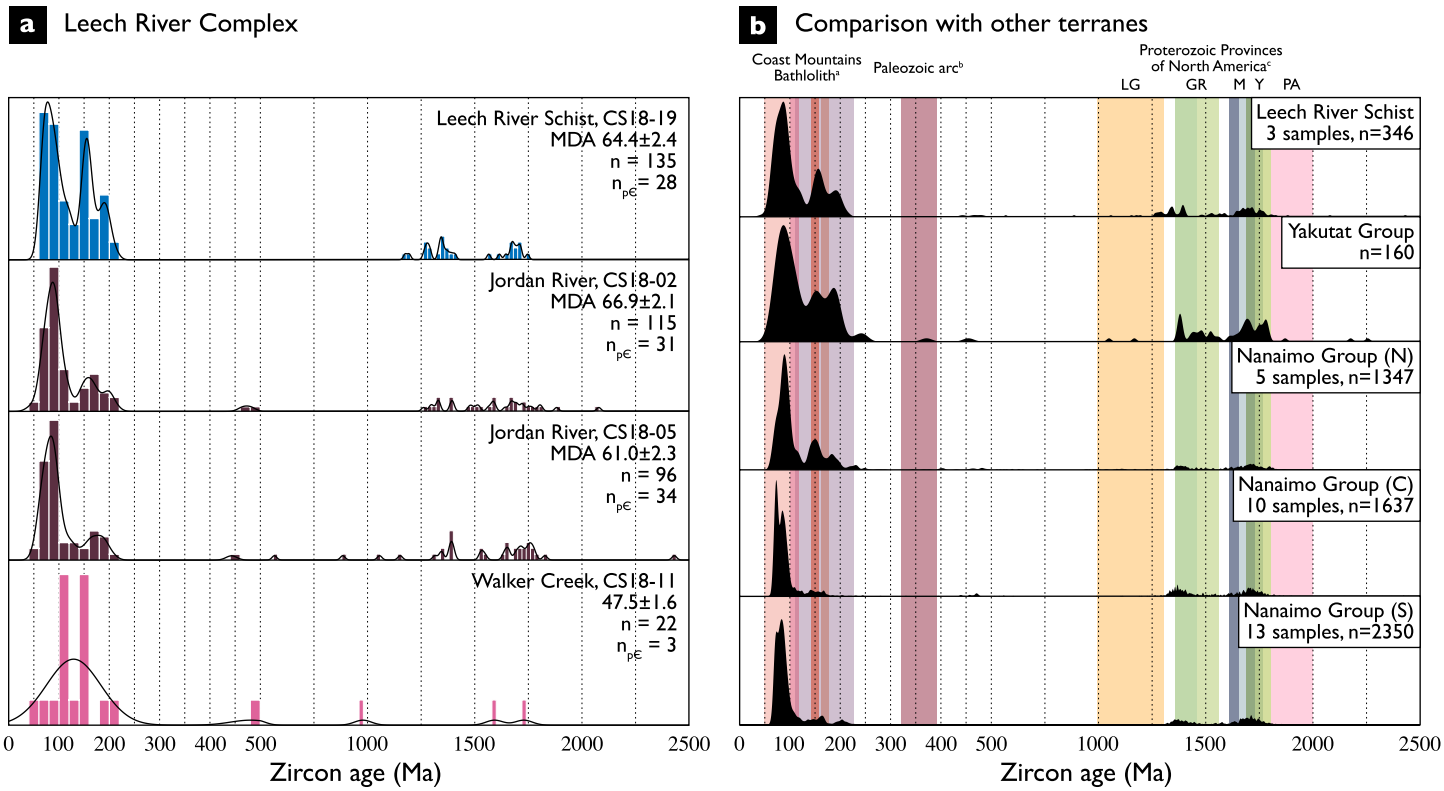


**Figure 3.** U-Pb detrital zircon geochronology of the Leech River Complex. (a) Histograms and kernel density estimates for detrital zircons from the Leech River Schist (LRS; CS1819, blue), Jordan River metasandstone (CS1802 and CS1805, purple), and the Walker Creek intrusions (CS1811, pink). Note that there is a break in scaling on the *x*-axis at 500 Ma but the bin size is consistently 20 Myr. (b) Detrital zircon age distributions (KDEs) from the LRS compared with the Yakutat Group (Garver & Davidson, 2015) and "Facies 2" zircons from the Upper Nanaimo Group (northern, central, and southern transects of Coutts et al. (2020), Englert et al. (2018), and Matthews et al. (2017)). Colored bars represent detrital zircon provenances from [a]Gehrels et al. (2009), [b]Nelson and Colpron (2007), and [c]Whitmeyer and Karlstrom (2007). LG—Llano-Grenville province. GR—Granite-Rhyolite province. M—Mazatzal province. Y—Yavapai province. PA—Paleoproterozoic arcs.

with two significant peaks at 60–100 and 140–200 Ma and a cluster of minor peaks between 1,100 and 1,800 Ma. Mesozoic zircons were likely sourced from the nearby Coast Mountains Batholith, the volcanic arc formed from Jurassic-Cretaceous subduction beneath the western margin of Wrangellia (Cecil et al., 2018; Friedman & Armstrong, 1995; Gehrels et al., 2009). Precambrian zircons have several possible sources, which are discussed below. The similar U-Pb age distribution and MDAs for the LRS and Jordan River Unit, together with petrographic observations (Figure S2 in Supporting Information S1), support the interpretation that the Jordan River Unit is metasedimentary (as defined by Fairchild and Cowan (1982) and Muller (1980)). The Walker Creek intrusion contains very few zircons. The youngest zircon age in the Walker Creek sample is 47.5 ± 1.6 Ma ($2\sigma$), which may represent a crystallization age but this is inconclusive. The Walker Creek age distribution matches distributions from the LRS and Jordan River metasandstone, suggesting these zircons were all inherited during in situ partial melting of the schist, consistent with the peraluminous compositions of the intrusions.

### 4.2. Metchosin Basalt (Footwall of the LRSZ)

The Metchosin Basalt is a very fine-grained to aphanitic amygdaloidal basalt composed of pyroxene or amphibole + plagioclase + epidote + titanite ± chlorite ± quartz. Near Sombrio Point, south of the shear zone, the basalt is massive with preserved volcanic textures, including several meter-scale pillows which contain amygdules. Pillows and pillow interstices contain patches of epidote-rich rock as well as abundant epidote veins (Figure 2f). There is no grain-scale or distributed foliation, so there is little evidence of pervasive deformation, but small faults with no preferred orientation are observed locally. The lack of consistent deformation fabrics in the basalt away from the LRSZ suggest that the basalt has experienced negligible distributed internal deformation.

## 5. Field and Microstructural Observations of the Leech River Shear Zone

In this section, we describe the structure, kinematics, and metamorphism of the LRSZ. Our study area is focused on 10s $m^2$ exposures predominantly located around the Diversion and Bear Creek reservoirs (Figure 1), with other exposures located in a region ~12 km along strike toward the coast.

### 5.1. Structure and Kinematics

The LRSZ is an approximately 600-m wide mylonitic shear zone that deformed both the LRS and the Metchosin Basalt. We define the LRSZ as a high strain zone that contains distinct mylonitic fabrics and kinematic indicators compared to the surrounding rocks. In the schist, the shear zone is characterized by planar and composite foliations, abundant deformed quartz veins, isoclinal folds with subhorizontal and steeply plunging fold axes, and a reduction in grain size (notably of porphyroblasts). In the metabasalt, the shear zone is characterized by planar foliation development and the presence of metamorphic amphibole. The edges of the LRSZ in both lithologies are gradational, and the mylonite zone is wider in the schist than in the metabasalt. The large-scale architecture of the shear zone, including potential lithologic mixing and deformation heterogeneity, is not well constrained due to limited exposure. A lithologic contact between the schist and metabasalt mylonites was only observed in the spillway between the reservoirs, where the contact is sharp and planar over the extent of the outcrop, which is ~10 m in length along strike.

The LRS mylonite is a strongly foliated and lineated, fine-grained rock (Figures 4a–4e). The mylonitic foliation is subparallel to the map-scale structure, striking approximately east-west and dipping steeply (average ~70°) to the north (Figure 1e). This foliation is defined by subparallel compositional layers, a composite S-C-C′ foliation within phyllosilicate-rich layers and a ubiquitous grain shape preferred orientation that is locally parallel to the compositional layers (Figures 1e, 4a–4d, 5a and 5b). Elongate grains and aggregates of aligned phyllosilicates on foliation planes define a penetrative, steeply plunging stretching lineation (Figures 1e and 4e). Compositional layers (millimeters to centimeters thick with rare ~10s-cm-thick layers) are differentiated by changes in the relative proportion of phyllosilicates, quartz, and feldspar, equivalent to the layering between metapsammitic and metapelitic lithologies north of the shear zone. These layers are typically planar and continuous for up to tens of centimeters to meters, with lengths limited by boudinage or exposure, such that the layering is extremely attenuated relative to outside the shear zone. Three types of folds affect the layering within the schist mylonite (Figure 1e). Isoclinal folds of the layering have axial planes parallel to the mylonitic foliation and both subhorizontal and steeply plunging hinges (Figures 4b and 4c). Tight folds of the layering are less common and have axial planes at a low angle to the foliation and steeply plunging axes subparallel to the stretching lineation (Figure 4f). Kink folds of the foliation are rare and have axial planes at a high angle to the foliation (Figure 4f). Asymmetry exhibited by all fold types is generally consistent with north-side up reverse shear in subvertical exposures and left-lateral shear in subhorizontal exposures. Shear bands that deflect the layering, boudin margins, and quartz veins define the C–C′ composite foliation. We interpret the mylonitic foliation ($S_3$) to be axial planar to isoclinal folds of $S_{0-2}$, which are all parallel due to transposition within the shear zone.

The Metchosin metabasalt mylonite contains a strong foliation defined by millimeter- to centimeter-scale compositional layering between plagioclase- and amphibole-rich layers (Figures 1e, 4g and 4h). Some compositional layers are boudinaged with boudin long axes parallel to the layering. At the grain-scale, large (~200 to 500 μm) asymmetric amphibole porphyroblasts are surrounded by a fine-grained amphibole, plagioclase, and sometimes epidote matrix (Figure 6). Amphibole, plagioclase ribbons, and subparallel trains of titanite and ilmenite grains all show shape-preferred orientations parallel to the compositional layering. Subparallel long axes of amphibole minerals define a steeply plunging, penetrative mineral lineation in the metabasalt mylonite (Figure 1e).

Quartz veins centimeters to tens of meters long are present in both the schist and metabasalt, though they are far more abundant in the schist mylonite. The range of shapes and attitudes of the veins indicates they were progressively deformed during noncoaxial deformation. Most veins are boudinaged into asymmetric shapes or are isoclinally folded with asymmetric geometries, with axial planes subparallel to the mylonitic foliation and steeply plunging hinges (Figures 1e and 4). A few veins exhibit folded axial surfaces, indicating they were refolded and likely formed relatively early in the deformation history. The latest veins are planar and crosscut the foliation at apparent angles of ~30° in subhorizontal exposures. Large sets of sheeted veins are tens of centimeters to around one m thick and can be traced for hundreds of meters along strike (Figure 4a). These sheeted veins are present in

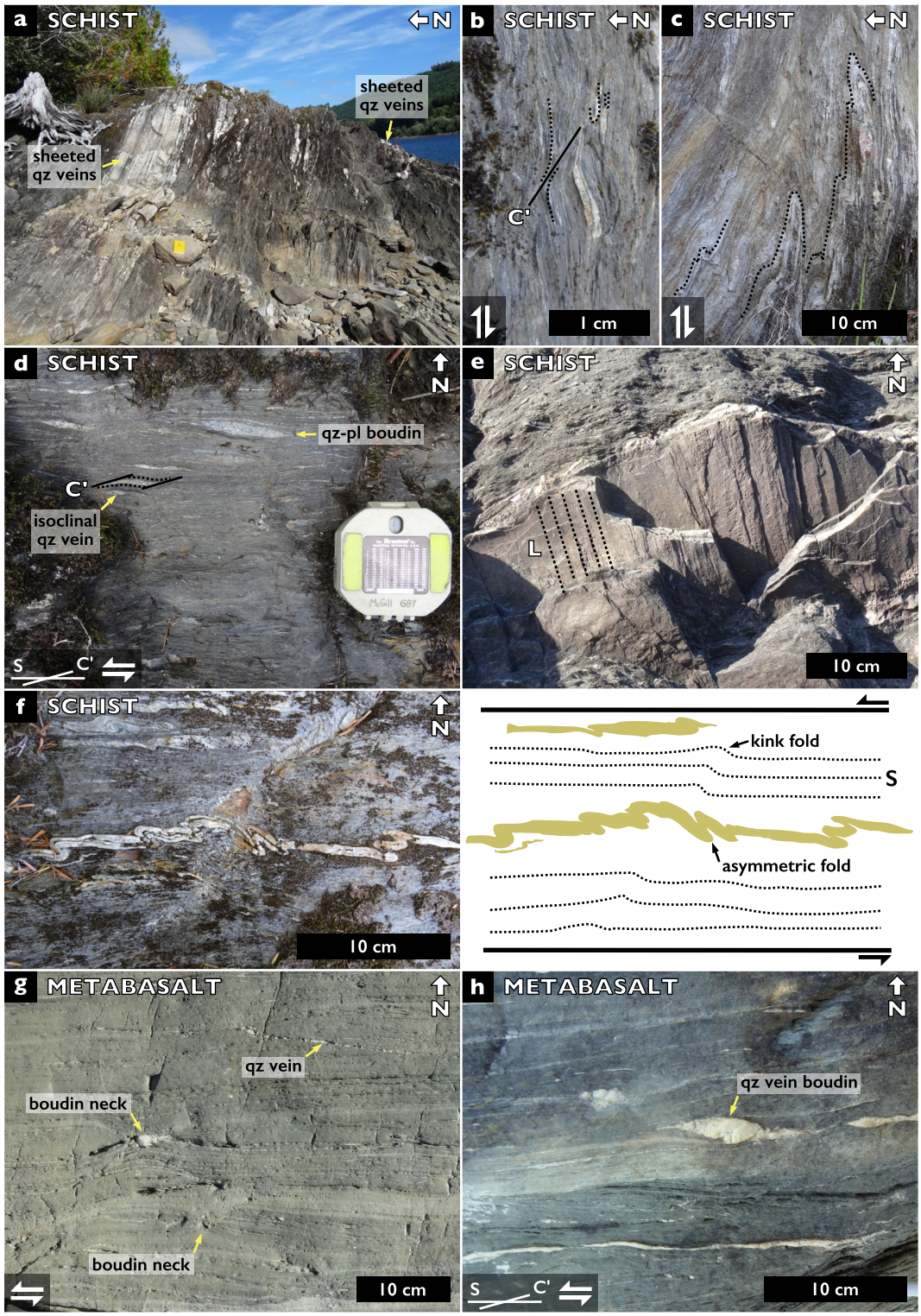


**Figure 4.**

both the schist and metabasalt mylonites and contain centimeter-thick layers of quartz separated by submillimeter layers of phyllosilicates or amphibole, respectively, interpreted as selvages of the local wall rock. They are also isoclinally folded with steeply dipping axial surfaces subparallel to the mylonitic foliation and are occasionally boudinaged.

Kinematic indicators observed in outcrop (Figure 4) and in thin section (Figures 5 and 6) in both the schist and metabasalt mylonites exhibit north-side-up reverse-sense kinematics in steeply dipping exposures and sections (i.e., perpendicular to the foliation and containing the lineation) and apparent sinistral kinematics when viewed in subhorizontal exposures (i.e., perpendicular to the lineation), with reverse-sense indicators most strongly expressed. Overall, the dominant reverse-sense indicators and steeply plunging lineation indicate predominantly thrust motion and secondary sinistral strike-slip motion, which is consistent with sinistral-oblique underthrusting of the Metchosin Basalt beneath the LRS.

### 5.2. Pressure and Temperature of Deformation

Pre- and synkinematic *P-T* conditions were determined with a combination of microstructural observations, mineral chemistry analyses, and phase equilibrium modeling. The schist mylonites in the LRSZ contain garnet + biotite + chlorite + muscovite + plagioclase + quartz + ilmenite ± rutile ± staurolite ± andalusite ± graphite (Figure 5). Compositional layering between millimeter- to centimeter-thick quartz-plagioclase-rich and phyllosilicate-rich layers dominates the microstructure (Figure 5a) with porphyroblasts of garnet, staurolite, and andalusite. Quartz grains exhibit interlobate grain boundaries and subgrain development indicative of crystal-plastic deformation via dislocation creep (Figure 5b). Garnet occurs within phyllosilicate-rich layers. Garnet porphyroblasts are euhedral, lack evidence of retrogression, and often have weakly asymmetric tails and pressure shadows of quartz and phyllosilicates in both lineation-parallel and lineation-perpendicular orientation (Figures 5c and 5d). Some garnet grains are inclusion-free, while others have ilmenite and/or quartz inclusions. Ilmenite grains are also dispersed within mica-dominated layers in the matrix and are aligned with their long axes parallel to foliation. Fine-grained rutile is also present and occurs as elongate grains parallel to the foliation. Andalusite porphyroblasts (~1- to 10-mm long) are fragmented, surrounded by reaction rims composed of muscovite and biotite, and have weakly asymmetric tails composed of chlorite, biotite, and muscovite (Figure 5e). Staurolite porphyroblasts are partially replaced by chlorite and quartz and also have weakly asymmetric tails (Figure 5f). Biotite porphyroblasts with their basal plane at an angle to the foliation are coarse-grained (~100 to 1,000s μm long), blocky, and often contain graphite interlayers (Figure 5g). Fine-grained biotite, chlorite, and muscovite are intergrown in phyllosilicate-rich layers with basal planes locally parallel to the foliation. These phyllosilicate-rich layers have variable proportions of each phase, and muscovite-chlorite layers are most common. The reaction rims around andalusite and staurolite porphyroblasts indicate disequilibrium with the matrix phases, and they are therefore likely prekinematic with respect to $S_3$. Some samples show snowball garnets, indicating that garnet, at least partially, grew synkinematically with $S_3$ (Figure 5d).

Garnet compositions were analyzed to establish the timing of garnet growth and define *P-T* conditions of metamorphism. Grain transects and compositional maps show zoning in all four garnet components (Figure 7 and Figure S3 in Supporting Information S1; Table S4). Spessartine content is at maximum in the cores ($Sps_{26}$) and decreases continuously through the mantles to a minimum of $Sps_{15}$ in the rims, typical of prograde growth. Almandine content increases continuously from $Alm_{58}$ in the cores up to $Alm_{69}$ in the rims. Both pyrope and grossular contents show a continuous zonation profile through the cores and mantles, with compositions of $Py_{7.5}Grs_6$ with $X_{Mg}$ at 0.11 in the cores to $Py_{10}Grs_4$ and $X_{Mg}$ at 0.13–0.14 in the mantles. Both of these components then show a sharp decrease or increase, respectively, in a thin, asymmetric rim, which can be observed most clearly in the Ca map. The composition of this rim is around $Alm_{69}Py_9Grs_6Sps_{15}$ with an $X_{Mg}$ of 0.12–0.13. The Ca map also shows growth zoning between the cores and mantles; however, the continuity from cores through mantles in the other maps indicates that some diffusion has likely contributed to smoothing the profiles. The thin rims are asymmetric with respect to the $S_3$ foliation, which indicates syn-$S_3$ growth of the rims. Garnet cores are therefore likely related to pre-$S_3$ metamorphism and rims related to shear zone deformation.

**Figure 4.** Field photos of structure and kinematics of the mylonite zone. Subvertical sections contain north-side-up shear sense indicators and subhorizontal sections contain left-lateral shear sense indicators. (a–c) Subvertical sections of the Leech River Schist mylonite showing foliation defined by compositional layering and alignment of phyllosilicate basal planes, C′ shear bands, isoclinal folding of quartz-dominated layers, and asymmetric folding of the foliation. (d) Subhorizontal section of the LRS mylonite showing foliation, C′ shear bands, boudinage of quartz- and plagioclase-dominated layers, and isoclinal folding of quartz-dominated layers. (e) Steeply plunging stretching lineation (L) visible on foliation planes within the LRS mylonite is defined by aligned mineral aggregates of phyllosilicates. (f) Subhorizontal section of the LRS mylonite showing asymmetric shear folding of a quartz- and plagioclase-dominated layer and kink folding of foliation (S). The schematic cartoon illustrates the two types of folds. (g and h) Subhorizontal sections of Metchosin Basalt mylonite showing foliation defined by compositional layering, C′ shear bands, and boudinage of compositional layering and quartz veins.

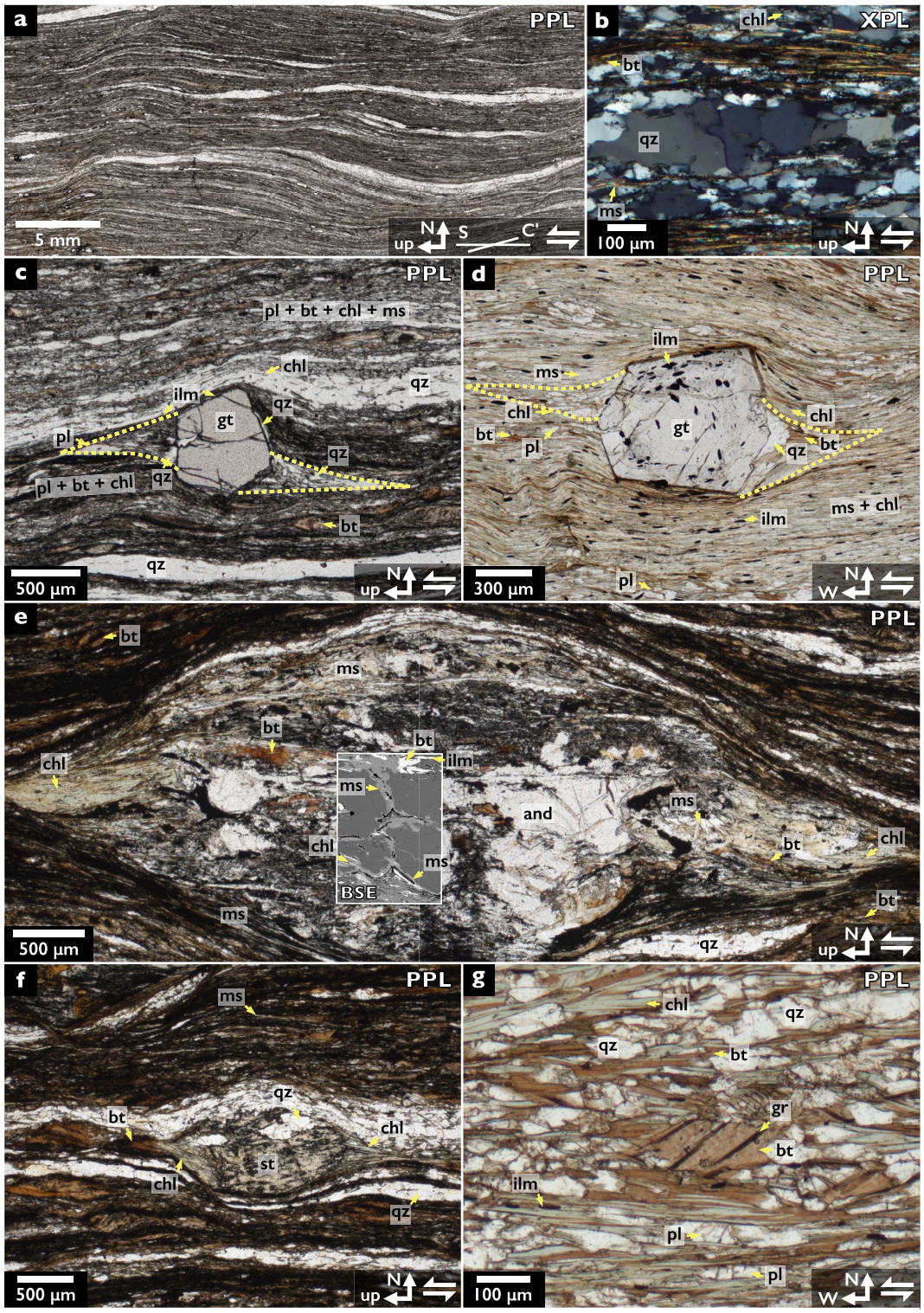


**Figure 5.** Leech River Schist mylonite microstructure. Photomicrographs in plane-polarized (PPL) and cross-polarized (XPL) light. (a) Foliation planes (S) defined by compositional layering deflected by C' shear bands creating an asymmetric composite foliation. (b) Quartz-dominated layer with interlobate quartz grain boundaries. (c) Garnet sigma-clast with asymmetric tails in lineation-parallel section. (d) Garnet sigma-clast with asymmetric tails and rotated ilmenite inclusions in lineation-perpendicular section. (e) Andalusite sigma-clast partially replaced by muscovite with asymmetric tails. (f) Staurolite sigma-clast partially replaced by chlorite with asymmetric tails. (g) Biotite porphyroblast with graphite inclusions and intergrown biotite and chlorite in a phyllosilicate-dominated layer. And—andalusite, bt—biotite, chl—chlorite, gr—graphite, gt—garnet, ilm—ilmenite, ms—muscovite, pl—plagioclase, qz—quartz, and st—staurolite.

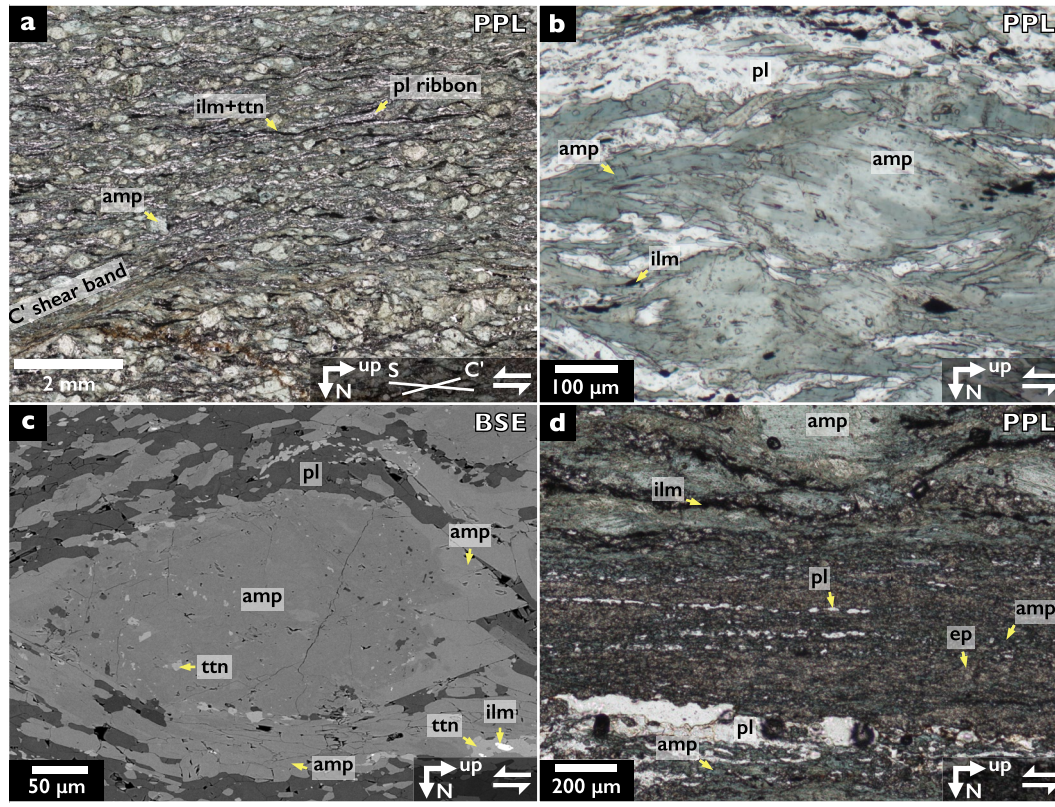


**Figure 6.** Metchosin Basalt mylonite microstructure. Photomicrographs in plane-polarized (PPL) and cross-polarized (XPL) light. (a) Foliation planes (S) deflected by both C planes, oriented horizontally, and C' shear bands creating an asymmetric composite foliation. (b and c) Chemical zoning between light green and dark green amphibole cores and tails. Fine-grained plagioclase surrounding amphibole porphyroblasts. Ilmenite seams along edges of amphibole domains. (d) Fine-grained epidote-amphibole layer. Amp—amphibole, ep—epidote, ilm—ilmenite, pl—plagioclase, and ttn—titanite.

Based on the mineral textures and garnet zoning, two mineral assemblages can be defined for determination of a *P-T* path; a pre-$S_3$ assemblage includes garnet (cores) + ilmenite + quartz ± andalusite ± staurolite and a syn-$S_3$ assemblage of garnet (rims) + biotite + chlorite + muscovite + quartz + ilmenite.

*P-T* conditions and a *P-T* path were established for metamorphism of the schist mylonite (sample CS18-32) using phase equilibrium modeling with the following solution models: Gt(HP), Chl(HP), Mica(CHA1), Bio(TCC), feldspar, St(HP), Ctd(HP), IlGkPy, and Ep(HP) (Auzanneau et al., 2010; Fuhrman & Lindsley, 1988; Holland & Powell, 1998; Tajčmanová et al., 2009). The modeled sample contains no graphite but apatite is present and therefore the corresponding amount of CaO bonded to $P_2O_5$ observed in the whole-rock analysis was subtracted from the bulk composition (Table S5 in Supporting Information S1). Since garnet cores (and mantles) and rims represent different metamorphic stages with respect to $S_3$, they were modeled in two separate *P-T* sections (Figure 8, Evans, 2004). Note that these calculations have an uncertainty of ±50°C (Palin et al., 2016; Powell & Holland, 2008). Garnet core and mantle *P-T* conditions were modeled in the system $MnO$-$Na_2O$-$CaO$-$K_2O$-$FeO$-$MgO$-$Al_2O$-$SiO_2$-$TiO_2$-$H_2O$ with $H_2O$ as a saturated phase (Figure 8a). Measured garnet core compositions match modeled garnet compositions at the garnet-in line between 525°C and 540°C and 340–370 MPa within the stability field Grt-Bt-Ms-Chl-Pl-Ilm-Qz, which is consistent with the presence of ilmenite inclusions in garnet cores. The increase in $X_{Mg}$ and almandine content and decrease in spessartine and grossular content from garnet cores through mantles indicate garnet growth during an increase in temperature to conditions of 550°C–565°C and 340–370 MPa. Measured garnet mantle compositions match modeled garnet isopleths in and around phase fields that include both andalusite and staurolite, suggesting that these two minerals grew concurrent with garnet mantle growth primarily related to heating.

To account for fractionation, garnet rims were modeled separately using a bulk composition from which garnet cores and mantles were removed (Figure 8b). Based on thin section observations and volume percentage predicted

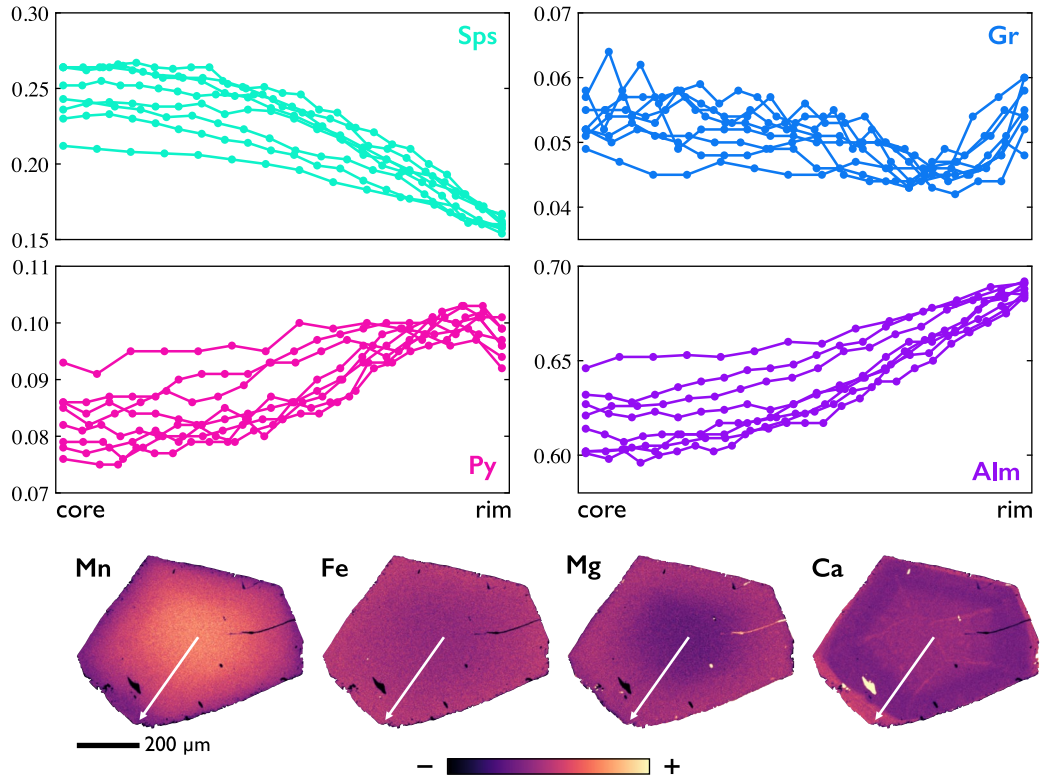


**Figure 7.** Garnet compositions from the schist mylonite. Garnet end-member fractions along core-to-rim transects (top) and representative wavelength-dispersive X-ray spectroscopy (WDS) maps (bottom) show garnet compositional zoning. In the cores and mantles, Mn and Ca content decreases and Mg and Fe content increases during growth. Then, in the rims, Ca and Mg content show a sharp change in thin, asymmetric rims. White arrows indicate location of microprobe transect. Sps—spessartine (Mn), Py—pyrope (Mg), Alm—almandine (Fe), and Gr—grossular (Ca).

by the *P-T* section for garnet cores and mantles, 0.45 vol% garnet with a composition averaged from garnet cores and mantles ($Alm_{61}Sps_{22}Py_9Grs_5$) was subtracted from the whole rock composition. Minor magnetite present in the matrix indicates the presence of ferric iron, and it is also therefore appropriate to consider the redox budget in the calculation. $O_2$ content was estimated from a T-$X_{O2}$ section at 400 MPa calculated for the new bulk composition (Figure S4 in Supporting Information S1). The stability of magnetite and the garnet rim compositions suggest that between 0.04 and 0.10 wt% $O_2$ may have been present in the system during shearing. We therefore added 0.07 wt% $O_2$ to the bulk composition to estimate *P-T* conditions of garnet rim growth and shearing.

The decrease in pyrope content and increase in grossular content in the garnet growth rims relative to the mantles indicate an increase in pressure during development of $S_3$, which destabilized andalusite and staurolite. The garnet rim compositions plot at the now higher temperature garnet-in line (from fractionation), recording *P-T* conditions of 550°C–570°C and 450–490 MPa with the following phases stable: Grt-Bt-Ms-Chl-Pl-Mag-Qz, which is consistent with the $S_3$ mineral assemblage (Figure 8b). Matrix biotite compositions ($X_{Mg}$ = 0.46–0.49) match corresponding isopleths that are mostly consistent with this garnet rim estimate, plotting at only slightly higher temperatures (570°C–590°C). This estimate indicates the peak pressure recorded by garnet growth related to shearing deformation, although the presence of minor rutile in the sample suggests conditions may have reached higher pressures (above 700–900 MPa). However, the lack of evidence of equilibration in other minerals makes these conditions impossible to estimate, but the *P-T* modeling shows a clear pattern of an initial phase of heating, followed by a near-isothermal pressure increase.

Peak temperature estimates were also calculated from the Ti content of biotite following the method of Henry et al. (2005). Biotite grains selected for geothermometry were inclusion-free, showed no retrogression textures, and were not in contact with garnet. The Ti contents suggest peak metamorphic temperatures were primarily between 550°C and 600°C with an error of ±24°C (Figure 9, Table S6). This temperature estimate is consistent

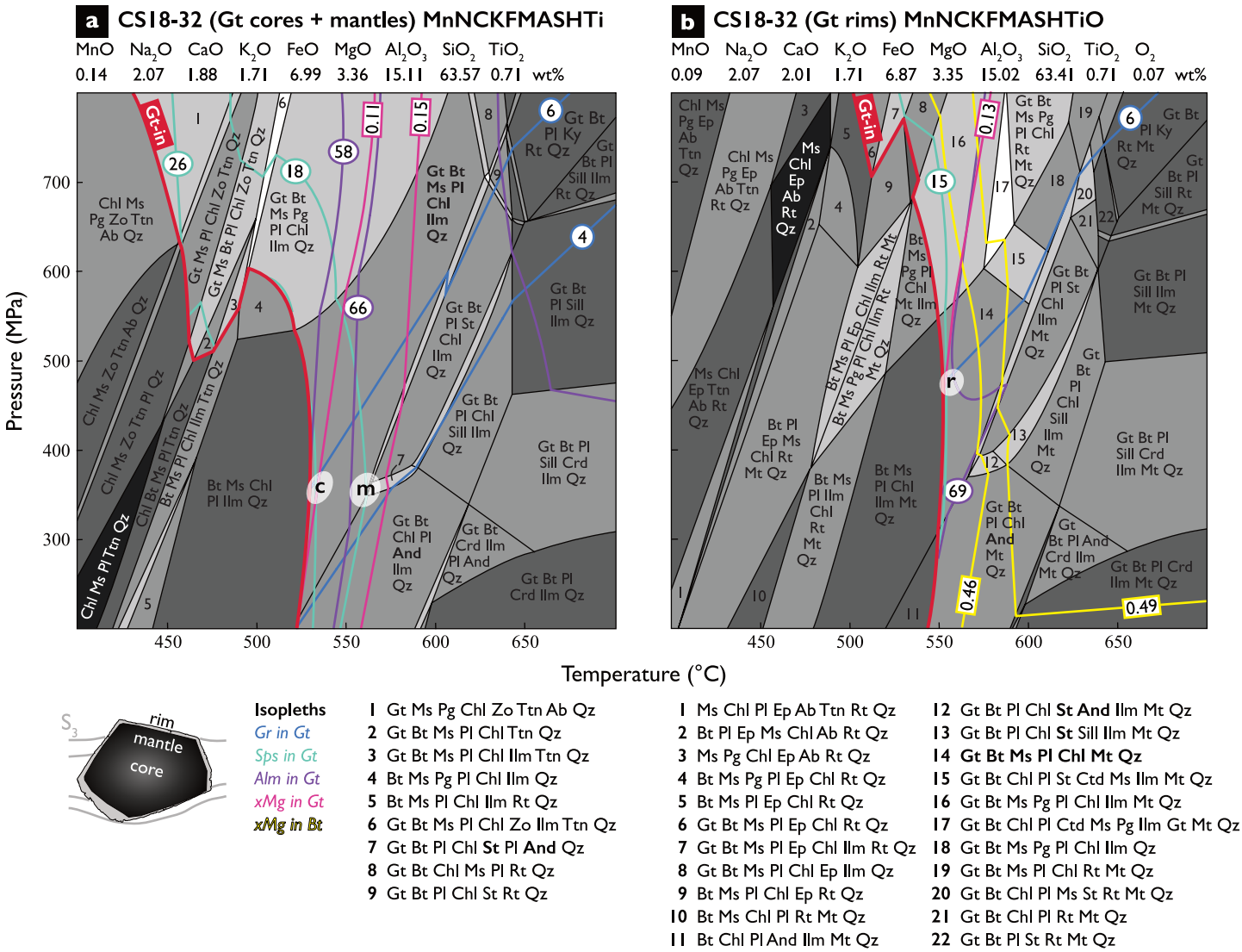


**Figure 8.** *P-T* section for schist mylonite. *P-T* sections generated for schist mylonite sample CS18-32 with contours of grossular (Gr), spessartine (Sps), and almandine (Alm) content as well as $X_{Mg}$ for garnet core, mantle, and rim compositions. (a) Garnet core compositions crossover at 525°C–540°C and 340–370 MPa, while mantle compositions crossover at 550°C–565°C and 340–370 MPa. (b) Garnet rim compositions crossover at 550°C–570°C and 450–490 MPa. Garnet cartoon illustrating the mylonitic foliation orientation and compositional zoning that defines the cores, mantles, and rims. Ab—albite, And—andalusite, Bt—biotite, Chl—chlorite, Crd—cordierite, Ep—epidote, Gt—garnet, Ilm—ilmenite, Ky—kyanite, Mt—magnetite, Pg—paragonite, Pl—plagioclase, Qz—quartz, Rt—rutile, Sill—sillimanite, St—staurolite, and Ttn—titanite.

across the four samples from the LRS mylonite and matches the temperature range predicted by the phase equilibrium modeling.

The metabasalt mylonites contain a synkinematic mineral assemblage of amphibole + plagioclase + epidote + titanite ± chlorite ± quartz. Large amphibole porphyroblasts have chemically distinct cores and tails (Figure 6b) and sometimes contain inclusions of titanite and plagioclase (Figure 6c). Fine-grained amphibole, plagioclase, epidote, titanite, and ilmenite surround the amphibole porphyroblasts. Titanite and ilmenite occur as discontinuous seams often wrapping around amphibole grains with titanite sometimes enveloping large ilmenite grains. Quartz and chlorite occur as minor phases, with quartz present as fine grains within the matrix and rare chlorite present along amphibole tails. Fine-grained layers of epidote and amphibole with interspersed ribbons of plagioclase may represent relict epidote veins (Figure 6d).

*P-T* conditions during metamorphism of the metabasalt mylonite were constrained with amphibole and plagioclase compositions (Figure 10, Tables S7 and S8). Spot analyses and maps document increasing Fe, Al, Ti, and

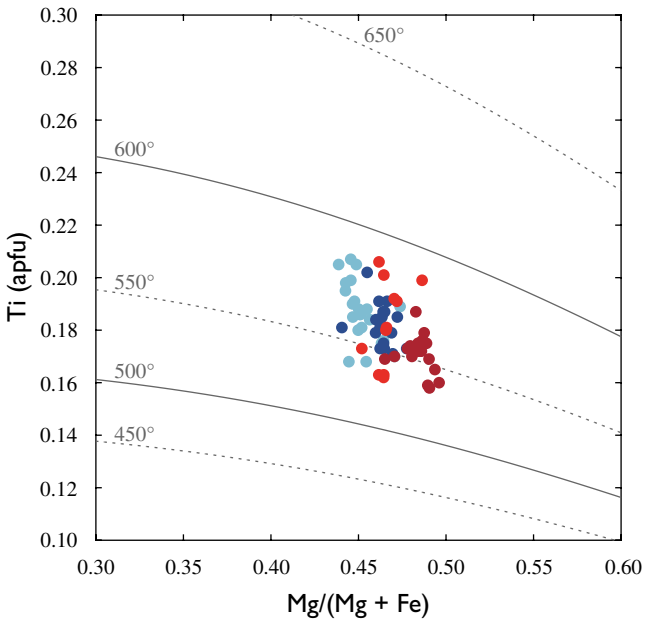


**Figure 9.** Ti-in-biotite thermometry. Ti content in biotite from the schist mylonite plotted on the Ti saturation surfaces of Henry et al. (2005). All analyses fall between the 500°C and 600°C contours.

Na content and decreasing Mg and Si content from amphibole cores to rims/tails (Figures 10a and 10c). The Si, Al, and Na distribution in amphibole structural sites depends on the pressure and temperature during growth (Ernst & Liu, 1998; Spear, 1981, 1995). Amphibole transitions from actinolite cores to hornblende/tschermakite rims via the pressure-sensitive Al-Tschermak substitution ($^{T}Si + {}^{M1\text{-}M3}Mg = {}^{T}Al + {}^{M1\text{-}M3}Al$). The positive correlation between A site occupancy and tetrahedrally coordinated Al ($Al^{iv}$) records the temperature-sensitive edenite exchange ($^{T}Si + {}^{A}[\ ] = {}^{T}Al + {}^{A}(Na + K)$). Growth of magnesio-hornblende amphibole rims suggests peak metamorphic temperatures were >420°C, providing a minimum constraint (Maruyama et al., 1983). Additionally, $TiO_2$ in amphibole increases from 0.05 to 0.15 in the cores to 0.20–0.50 in the rims. The increasing $TiO_2$ content is consistent with increasing temperature (Ernst & Liu, 1998). These trends record prograde amphibole growth during deformation. Metamorphic plagioclase compositions are oligoclase to andesine ($An_{26–45}$; Figure 10b), which are typical of amphibolite facies metamorphism and the calcification of plagioclase, caused by increasing temperature, is consistent with the actinolite-to-hornblende transition (Maruyama et al., 1982, 1983; Spear, 1995).

## 6. Discussion

### 6.1. The Leech River Shear Zone: A Paleo-Subduction Thrust

Our field and microstructural observations are the first to document reverse-sinistral displacement across the LRSZ and define the LRSZ as a high strain zone distinct from the surrounding rocks. The kinematic interpretation is based on the steeply plunging lineation, north-side-up reverse-sense kinematic indicators in subvertical exposures and sinistral-sense indicators in subhorizontal exposures. We interpret the thinner, more repetitive compositional layering, composite foliations, and finer grain size in the schist mylonite to be the result of higher shear strain accumulated during further isoclinal folding, layer thinning, and transposition relative to the folding and disruption of bedding observed in the schist north of the LRSZ. The $S_2$ foliation in the LRS north of the mylonite zone is parallel to the mylonitic foliation ($S_3$) in both the schist and metabasalt mylonites, and the vergence direction throughout the schist and within the mylonite zone is similar, indicating that deformation of the entire package involved one predominant shortening direction with higher strain localized in the LRSZ. These interpretations are broadly consistent with previous observations (Fairchild & Cowan, 1982; Groome et al., 2003), though our results establish the importance of the reverse-sense motion across the LRSZ.

Metamorphic conditions in the schist and metabasalt mylonites in the LRSZ are consistent with deformation at amphibolite facies. In the schist mylonites, metamorphism involved an initial phase of heating at low pressure to amphibolite facies conditions, resulting in the prekinematic growth of biotite, staurolite, andalusite, and garnet (cores and mantles), followed by a sharp increase in pressure, resulting in the destabilization of staurolite and andalusite and synkinematic growth of muscovite, chlorite, biotite, and garnet (rims). This progression outlines a qualitative anticlockwise *P-T* path. Temperature and pressure estimates of 550°C–570°C and 450–490 MPa from garnet rim compositions (Figure 8) are further supported by peak temperature estimates of 550°C–575°C from Ti-in-biotite geothermometry (Figure 9). In the metabasalt mylonites, the transition from actinolite cores to hornblende rims in porphyroclasts indicates the transition from greenschist to amphibolite facies (Figure 10). Similar *P-T* conditions during synkinematic mineral growth in both the schist and metabasalt mylonites demonstrate that strain caused by reverse-sense motion was distributed across both units at peak *P-T*.

The metamorphic mineralogy of the schist and metabasalt mylonites is consistent with previous observations of the LRS and Metchosin Basalt from outside the LRSZ (Fairchild & Cowan, 1982; Groome et al., 2003; Rusmore & Cowan, 1985; Timpa et al., 2005). However, previous *P-T* estimates for the LRS were restricted to high-temperature, low-pressure metamorphism based on the presence of andalusite (Fairchild & Cowan, 1982; Groome et al., 2003). Our observations show that andalusite in the schist mylonite is rare, small (<1 cm), and exhibits disequilibrium textures, with chlorite and muscovite replacing andalusite and forming synkinematic tails (e.g., Figure 5e). We therefore interpret andalusite growth to predate synkinematic metamorphism in the LRSZ,

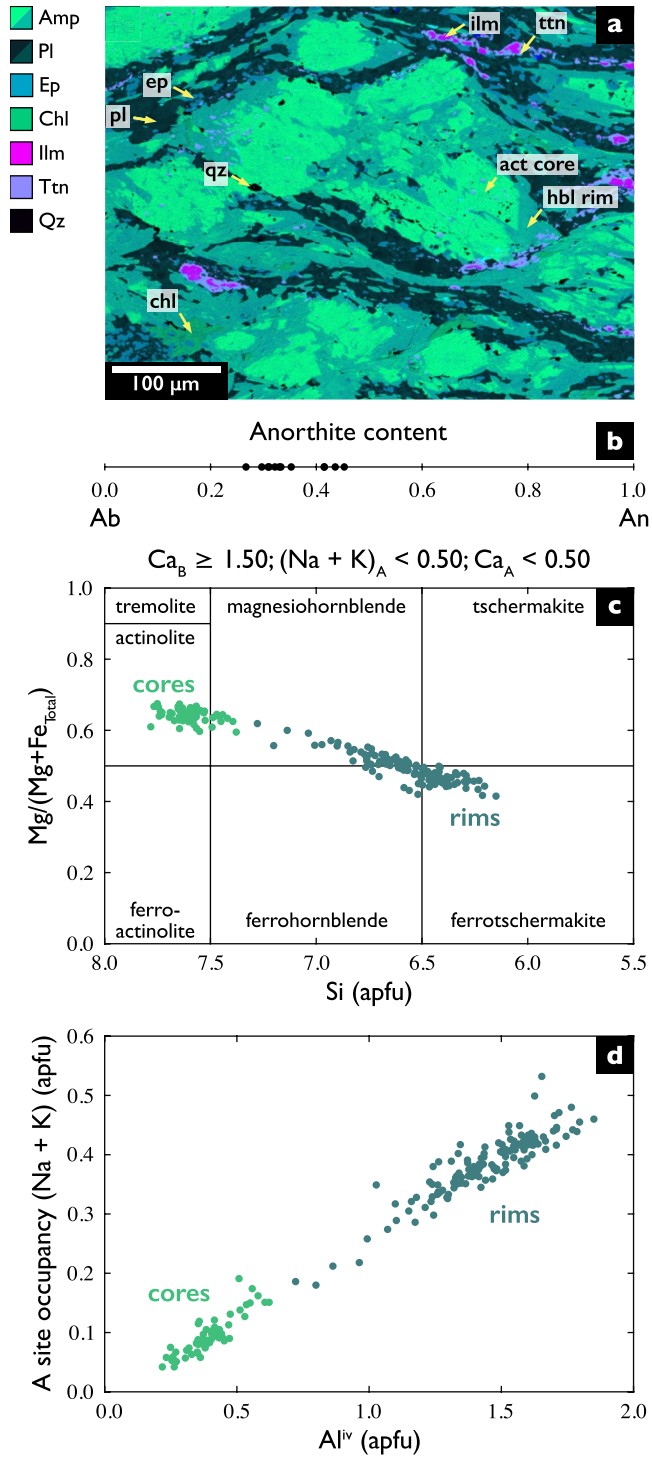


**Figure 10.** Amphibole and plagioclase compositions from the metabasalt mylonite. Chemical maps and point analyses from plagioclase grains and amphibole grains with chemically distinct cores and rims. (a) False-colored phase map generated from multiple x-ray maps highlighting chemically distinct cores and rims. Rim compositions extend into synkinematic tails. (b) Plagioclase compositions in the matrix range from $An_{27}$ to $An_{45}$. (c) Amphibole core and rim compositions plotted onto a discrimination diagram with field labels following Leake et al. (1997). Cores primarily plot as actinolite, while rims plot as hornblende to tschermakite. (d) Temperature-sensitive A site occupancy and pressure-sensitive tetrahedral alumina content demonstrate prograde growth of amphibole.

which is associated with a pressure increase of at least 100–200 MPa, or higher, based on the presence of rutile. This increase in burial depth after the high *T*, low P metamorphism suggests upper plate thickening associated with the underthrusting of the MIC occurred before and during the final docking of the MIC basalts in their current position relative to the structurally overlying LRC.

*P-T* estimates for the schist mylonites correspond to a geothermal gradient of ~30°C/km when the LRSZ was active, which is higher than the hottest modern subduction zones (Penniston-Dorland et al., 2015; Syracuse et al., 2010). However, geothermal gradients as high as 50°C/km during ridge subduction have been reported in other subduction complexes (e.g., Brown, 1998; Pavlis & Sisson, 1995; Sakaguchi, 1996; Sisson et al., 1989; Zumsteg et al., 2003). The elevated temperatures estimated from the LRSZ are likely due to the anomalously high geothermal gradients produced by subduction of the Kula/Resurrection-Farallon Ridge beneath the forearc, the young age of the subducting plate, and the nearby Yellowstone hotspot (Breitsprecher et al., 2003; Groome & Thorkelson, 2009).

The southward increase in metamorphic grade from greenschist to amphibolite facies in the LRS does not exhibit the inverted thermal gradient typical of subduction systems (Peacock, 1987). We suggest that the regional thermal structure of the LRC was established by heating from below by a young, hot, plume-affected oceanic plate, rather than refrigeration by a cold slab. Throughout the LRC, isoclinal, asymmetric folds with top-to-the-south vergence appear to have developed either prior to and/or at the local peak conditions, representing regional shortening during burial. The consistency of the attitudes of the $S_2$ regional foliation with the $S_3$ mylonitic foliation suggests this shortening could have occurred within the upper plate during convergence. The late near-isothermal increase in pressure recorded by the mylonites was likely due to tectonic burial by wedge shortening and thickening during underthrusting as strain localized onto the LRSZ. This interpretation implies the noncoaxial deformation in the LRSZ during the synkinematic growth of garnet rims only records the latest phase in the subduction history of the MIC as it progressed from the trench to peak *P-T* conditions.

Overall, the shear zone kinematics and anticlockwise *P-T* path with heating followed by a pressure increase, combined with the juxtaposition of a fragment of oceanic crust against an underplated terrigenous complex, all suggest that the LRSZ is a sinistral-oblique thrust that accommodated underthrusting of the Siletz-Crescent terrane beneath the North American margin in a subduction zone setting. The kinematics and synkinematic prograde metamorphic conditions inferred in both lithologies within the LRSZ are inconsistent with alternative hypotheses for the LRSZ tectonic setting (i.e., dominantly strike-slip motion (e.g., Fairchild & Cowan, 1982) or development as part of a forearc rift (e.g., Babcock et al., 1992)). Although the thermal history of the LRSZ is atypical of subduction assemblages, we conclude that the LRSZ represents a hot paleo-subduction interface.

### 6.2. Tectonic History of the Leech River Complex and Leech River Shear Zone

The LRSZ forms the tectonic contact between the LRC and MIC of the Siletz-Crescent terrane and therefore its deformation history can be used to inform the tectonic history of the surrounding units. Our results provide new constraints on the origin of the LRC. Detrital zircon U-Pb ages indicate an early Paleocene MDA for the Leech River Schist and Jordan River Unit of the LRC, which is significantly younger than previously reported Late Jurassic to Cretaceous deposition estimates based on whole-rock Rb-Sr isotopic data (Fairchild & Cowan, 1982) and youngest zircon U-Pb ages (Groome et al., 2003). These new ages for the LRC place an upper bound on when the LRSZ was active, and they are broadly consistent with underthrusting of the MIC in the Eocene (Eddy et al., 2017).

Detrital zircon age distributions from the LRC provide further constraints on its depositional context and further tests whether the LRC is an allochthonous terrane. The LRC has a similar age distribution to two groups of sedimentary rocks: the youngest (Maastrichtian to early Paleocene age) formations in the Upper Nanaimo Group on Vancouver Island (Coutts et al., 2020; Englert et al., 2018; Matthews et al., 2017) and the Yakutat Group in Alaska, which has previously been correlated with the Pacific Rim terrane (Garver & Davidson, 2015). The Upper Nanaimo Group was deposited in a marine subduction forearc basin (Coutts et al., 2020). The Yakutat Group, part of the Chugach-Prince William terrane, was deposited as trench-fill turbidites, then incorporated into an accretionary complex (Garver & Davidson, 2015). The LRC shares similar MDA, peaks in Proterozoic ages at 1,850–1,560 Ma and 1,450–1,300 Ma, and absence of grains with 1,000–1,300 Ma ages with these units (Figure 3b). For both the Upper Nanaimo Group and Yakutat Group, previous work interpreted detrital

zircon grains with Mesozoic and early Paleocene ages (200–60 Ma) to be derived from the Coast Mountains Batholith, while Proterozoic (1,850–1,560 and 1,450–1,300 Ma) zircons were interpreted to be sourced from the Yavapai and Mazatzal terranes of southwestern Laurentia (Coutts et al., 2020; Dumitru et al., 2016; Garver & Davidson, 2015; Housen & Beck, 1999; Matthews et al., 2017). It is important to note that the source of these Proterozoic-age zircons and the paleolatitude of the Nanaimo Group is an ongoing debate. However, we suggest these interpretations of detrital zircon source regions are also applicable to the LRC.

The LRC was previously interpreted as allochthonous to Vancouver Island (Fairchild & Cowan, 1982), but these new detrital zircon ages support an alternative interpretation. We suggest the similar detrital zircon age distributions (and therefore similar sources) of the LRC and Upper Nanaimo Group as it demonstrate that these units were derived from similar sedimentary sources and therefore likely deposited near each other in the latest Cretaceous to early Paleocene. This model also implies that the LRC was deposited in proximity to the Wrangellia terrane, which constitutes the majority of Vancouver Island, as the Nanaimo Group uncomfortably overlies the Wrangellia terrane (Mustard, 1994). Our data do not directly test whether there has been any relative motion between the LRC and Wrangellia; however, the simplest explanation for the similarity between the LRC and Nanaimo Group ages is that the LRC represents a marine sequence that shared the same source region at the same time as the Nanaimo Group basin. This tectonic context, the mixed lithologies of the LRC (psammitic, pelitic, and mafic volcanics), and the similar depositional age of the Upper Nanaimo suggest the LRC represents an assemblage of metamorphosed marine basin rocks, likely deposited in a near-margin trench environment. Within the LRC, the structural record of block-in-matrix textures, transposition of bedding, and layer-perpendicular veins are typical of underthrust subduction complexes (e.g., Connelly, 1978; Fisher & Byrne, 1987; Pavlis & Sisson, 1995; Meneghini et al., 2009; Ujiie, 2002). Furthermore, the LRS depositional age is broadly correlative with the Chugach accretionary complex and possibly parts of the Franciscan complex, which together record subduction off the west coast of North America in the latest Cretaceous and Paleocene (Cowan, 1982, 2003; Garver & Davidson, 2015). We therefore conclude that the LRC is not as an allochthonous terrane but represents an accretionary complex developed from trench-fill sediments consistent with the North American margin.

We summarize our results with available timing constraints on the tectonic history of the LRC, Siletz-Crescent, and LRSZ from the literature (Figure 11). At ~65 to 60 Ma (Figure 11a), the LRS (MDA ~66 to 61 Ma) and Upper Nanaimo Group (MDA ~80 to 64 Ma) were deposited in near-margin trench and forearc basins, respectively, with the Nanaimo Group unconformably overlying the Wrangellia terrane (this study; Coutts et al., 2020; Englert et al., 2018; Matthews et al., 2017). Any northward coast-wise transport of all three units occurred during oblique subduction (Coutts et al., 2020; Matthews et al., 2017). At ~52 Ma (Figure 11b), the Metchosin Basalt was erupted as part of an oceanic plateau (U-Pb zircon age of 52 ± 2 Ma; Massey, 1986), while the LRC was underthrust and deformed as an accretionary complex during subduction of the Kula/Resurrection and Farallon plates, and the Nanaimo Group was shallowly buried (Stewart & Page, 1974). The Kula/Resurrection-Farallon ridge (and slab window) was subducted ahead of the Metchosin Basalt. By ~51 to 48 Ma (Figure 11c), during the accretion of the Siletz-Crescent terrane to the North American margin (Eddy et al., 2017), the Metchosin Basalt was subducted beneath the LRS along the LRSZ, and the Cowichan fold-and-thrust belt developed in the Nanaimo Group (England & Calon, 1991). Shortening and thickening of the upper plate buried the active LRSZ, causing a near-isothermal pressure increase during shear. Shortly thereafter, the Metchosin Basalt and the LRSZ itself were underplated and accreted to the overriding continent as the décollement stepped further west. Emplacement of the Walker Creek intrusions pin the location of the schist to its current latitude from ~51 Ma to the present (Breitsprecher et al., 2003; Groome et al., 2003). Additionally, some of these intrusions exhibit deformation while others are not deformed (Groome et al., 2003), indicating syn- to postkinematic emplacement and marking the cessation of deformation in the LRSZ and underplating of the Metchosin Basalt. Following underplating, the LRC was exhumed through the mica cooling temperatures ($^{40}Ar/^{39}Ar$ ages of 45.2 ± 0.2 and 42.5 ± 0.2 Ma in muscovite and biotite, respectively; Groome et al., 2003). Exhumation may have been accommodated by a structurally lower fault during subsequent subduction (e.g., at the base of the MIC), though this is currently untested. Unconformable deposition of the coastal marine Carmanah Group across the LRSZ in the Oligocene constrains the exposure of the units at the surface (Figure 11d; Harrichhausen, 2021; Muller, 1977a). The compatibility of this reinterpretation with previous work on the tectonic history and timing of accretion of the Siletz-Crescent terrane (Eddy et al., 2016; Groome et al., 2003; McCrory & Wilson, 2013; Wells et al., 2014) reinforces the interpretation that the LRSZ was a hot subduction plate boundary interface in the Eocene.

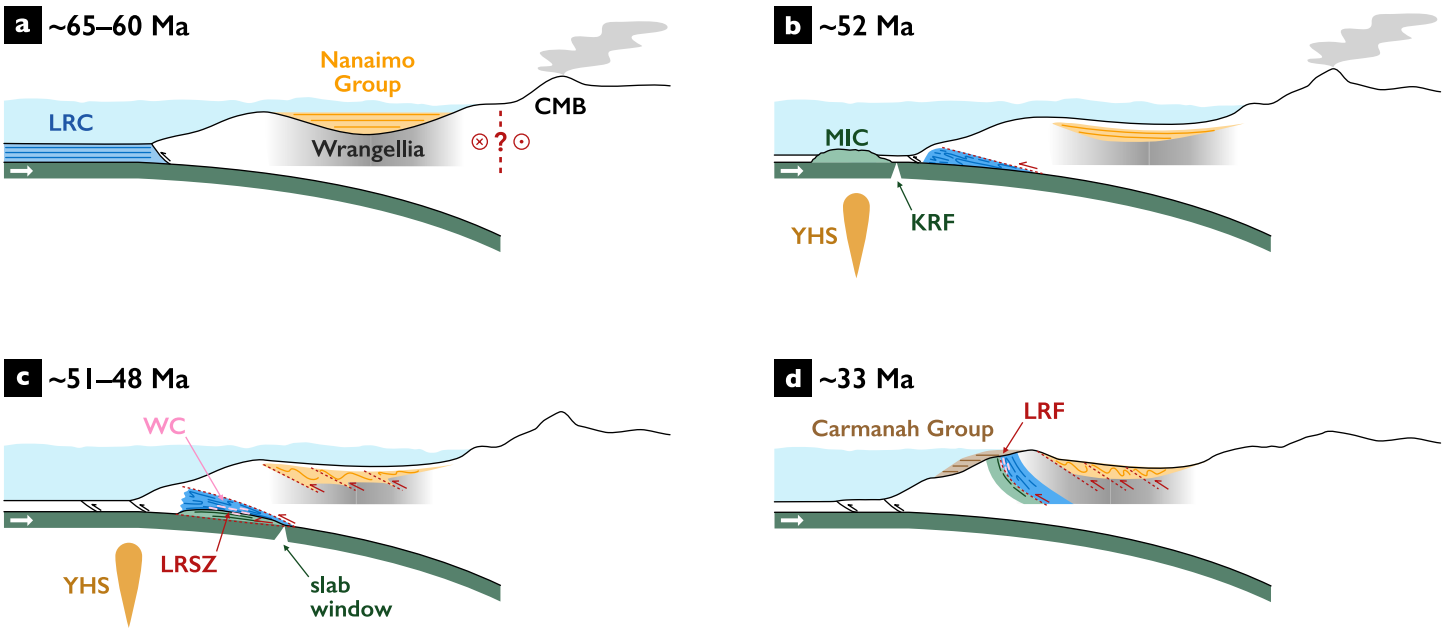


**Figure 11.** Tectonic history of the LRC, MIC, and LRSZ. Schematic cartoon (not to scale) of the development of the Leech River Shear Zone and surrounding terranes from ~65 to ~33 Ma. (a) Synchronous deposition of the Leech River Complex and Nanaimo Group, possibly at southern latitudes and followed by northward coast-wise translation. (b) Formation of the MIC as an oceanic plateau on the subducting oceanic plate near the Kula/Resurrection-Farallon ridge and Yellowstone hotspot. Deformation of the LRC as part of the accretionary complex. Shallow burial of the Nanaimo Group. Subduction of the Kula/Resurrection-Farallon ridge ahead of the MIC. (c) Deformation within the LRSZ accommodating subduction of the MIC beneath the LRC, slab window formation and emplacement of the Walker Creek intrusions, and formation of the Cowichan Fold-and-Thrust belt. (d) Exhumation of the LRC and MIC to the surface where the Oligocene-age Carmanah Group is uncomfortably deposited on top of the LRF in a coastal marine environment. CMB—Coast Mountains Batholith. KRF—Kula/Resurrection-Farallon ridge (slab window). LRC—Leech River Complex. LRF—Leech River Fault. LRSZ—Leech River Shear Zone. MIC—Metchosin Igneous Complex. WC—Walker Creek intrusions. YHS—Yellowstone Hotspot.

## 7. Conclusions

This study evaluates the LRSZ as a possible paleo-subduction interface. Structural, kinematic, and petrologic evidence from the LRSZ indicates hot rocks underwent reverse-sinistral sense deformation during a near-isothermal pressure increase at amphibolite facies conditions related to underthrusting during subduction. The elevated geothermal gradient implied by the *P-T* conditions likely resulted from subduction of the Kula/Resurrection-Farallon Ridge, subsequent formation of a slab window, and the nearby Yellowstone Hotspot. These observations are consistent with tectonic models of the hotspot location and plate motions during the Eocene (~50 Ma). Detrital zircon age distributions suggest the LRS is a Paleocene-age accretionary complex that was deposited in proximity to the Upper Nanaimo Group and Wrangellia terrane, and therefore the LRC is not allochthonous to Vancouver Island. Overall, we establish that the LRSZ represents a paleo-subduction interface from an anomalously hot Eocene subduction zone.

## Data Availability Statement

The whole rock compositional data, mineral composition data, detrital zircon U-Pb analyses, and structural data are available in the supplementary information. The geochemical data (whole rock, mineral, and detrital zircon U-Pb) are also available through the EarthChem (Seyler et al., 2022, https://doi.org/10.26022/IEDA/112312). *PerpleX* version 6.9.9 (Connolly, 2005) was used for phase equilibrium modeling and is developed openly at https://www.perplex.ethz.ch/.

**Acknowledgments**
The authors thank TimberWest and Hydro BC for assistance in accessing the field area. C.S. acknowledges support from the Fonds de recherche du Québec—Nature et technologies (FRQNT). J.K. acknowledges support from the Natural Sciences and Engineering Research Council of Canada (NSERC), Discovery Grant RGPIN-2022-04193. D.S. acknowledges support from an NSERC Undergraduate Student Research Award (USRA). A.L. acknowledges support from the University of Washington and thanks Tamas Ugrai and Samuel Shekut for assistance in the lab. C.R. acknowledges support from NSF EAR IRFP Grant #1349586 and NSF EAR Tectonics Grant #1756834. Thanks to Sarah Roeske, Cailey Condit, Peter Lindquist, and an anonymous reviewer.

## References

Auzanneau, E., Schmidt, M. W., Vielzeuf, D., & Connolly, J. A. D. (2010). Titanium in phengite: A geobarometer for high temperature eclogites. *Contributions to Mineralogy and Petrology*, *159*(1), 1–24. https://doi.org/10.1007/s00410-009-0412-7

Babcock, R. S., Burmester, R. F., Engebretson, D. C., Warnock, A., & Clark, K. P. (1992). A rifted margin origin for the crescent basalts and related rocks in the northern Coast Range Volcanic Province, Washington and British Columbia. *Journal of Geophysical Research*, *97*(B5), 6799–6821. https://doi.org/10.1029/91JB02926

Behr, W. M., Holt, A. F., Becker, T. W., & Faccenna, C. (2022). The effects of plate interface rheology on subduction kinematics and dynamics. *Geophysical Journal International*, *230*(2), 796–812. https://doi.org/10.1093/gji/ggac075

Breitsprecher, K., Thorkelson, D. J., Groome, W. G., & Dostal, J. (2003). Geochemical confirmation of the Kula-Farallon slab window beneath the Pacific Northwest in Eocene time. *Geology*, *31*(4), 351–354. https://doi.org/10.1130/0091-7613(2003)031<0351:GCOTKF>2.0.CO;2

Brown, M. (1998). Ridge–trench interactions and high-T–low-P metamorphism, with particular reference to the Cretaceous evolution of the Japanese Islands. *Geological Society, London, Special Publications*, *138*(1), 137–169. https://doi.org/10.1144/GSL.SP.1996.138.01.09

Cecil, M. R., Rusmore, M. E., Gehrels, G., Woodsworth, G., Stowell, H. H., Yokelson, I. N., et al. (2018). Along-strike variation in the magmatic tempo of the Coast Mountains Batholith, British Columbia, and implications for processes controlling episodicity in arcs. *Geochemistry, Geophysics, Geosystems*, *19*(11), 4274–4289. https://doi.org/10.1029/2018GC007874

Chelle-Michou, C., McCarthy, A., Moyen, J.-F., Cawood, P. A., & Capitanio, F. A. (2022). Make subductions diverse again. *Earth-Science Reviews*, *226*, 103966. https://doi.org/10.1016/j.earscirev.2022.103966

Clowes, R. M., Brandon, M. T., Green, A. G., Yorath, C. J., Brown, A. S., Kanasewich, E. R., & Spencer, C. (1987). LITHOPROBE—southern Vancouver Island: Cenozoic subduction complex imaged by deep seismic reflections. *Canadian Journal of Earth Sciences*, *24*(1), 31–51. https://doi.org/10.1139/e87-004

Connelly, W. (1978). Uyak complex, Kodiak Islands, Alaska: A Cretaceous subduction complex. *The Geological Society of America Bulletin*, *89*(5), 755–769. https://doi.org/10.1130/0016-7606(1978)89<755:UCKIAA>2.0.CO;2

Connolly, J. A. D. (2005). Computation of phase equilibria by linear programming: A tool for geodynamic modeling and its application to subduction zone decarbonation. *Earth and Planetary Science Letters*, *236*(1–2), 524–541. https://doi.org/10.1016/j.epsl.2005.04.033

Coutts, D., Matthews, W. A., Englert, R. G., Brooks, M. D., Boivin, M.-P., & Hubbard, S. (2020). Along-strike variations in sediment provenance within the Nanaimo basin reveal mechanisms of forearc basin sediment influx events. *Lithosphere*, *12*(1), 180–197. https://doi.org/10.1130/L1138.1

Cowan, D. S. (1982). Geological evidence for post-40 m.y. B.P. large-scale northwestward displacement of part of southeastern Alaska. *Geology*, *10*(6), 309–313. https://doi.org/10.1130/0091-7613(1982)10<309:GEFPMB>2.0.CO;2

Cowan, D. S. (2003). Revisiting the Baranof-Leech River hypothesis for early Tertiary coastwise transport of the Chugach-Prince William terrane. *Earth and Planetary Science Letters*, *213*(3–4), 463–475. https://doi.org/10.1016/S0012-821X(03)00300-5

Cowan, D. S., Brandon, M. T., & Garver, J. I. (1997). Geologic tests of hypotheses for large coastwise displacements—A critique illustrated by the Baja British Columbia controversy. *American Journal of Science*, *297*(2), 117–173. https://doi.org/10.2475/ajs.297.2.117

Cui, Y., Miller, D., Schiarizza, P., & Diakow, L. J. (2017). *British Columbia digital geology* (British Columbia Geological Survey Open File 2017-8, Data version 2019-12-19). British Columbia Ministry of Energy, Mines and Petroleum Resources.

DeLong, S. E., Schwarz, W. M., & Anderson, R. N. (1979). Thermal effects of ridge subduction. *Earth and Planetary Science Letters*, *44*(2), 239–246. https://doi.org/10.1016/0012-821X(79)90172-9

Dumitru, T. A., Elder, W. P., Hourigan, J. K., Chapman, A. D., Graham, S. A., & Wakabayashi, J. (2016). Four Cordilleran paleorivers that connected Sevier thrust zones in Idaho to depocenters in California, Washington, Wyoming, and, indirectly, Alaska. *Geology*, *44*(1), 75–78. https://doi.org/10.1130/G37286.1

Duncan, R. A. (1982). A captured island chain in the Coast Range of Oregon and Washington. *Journal of Geophysical Research*, *87*(B13), 10827–10837. https://doi.org/10.1029/JB087iB13p10827

Eddy, M. P., Bowring, S. A., Umhoefer, P. J., Miller, R. B., McLean, N. M., & Donaghy, E. E. (2016). High-resolution temporal and stratigraphic record of Siletzia's accretion and triple junction migration from nonmarine sedimentary basins in central and western Washington. *The Geological Society of America Bulletin*, *128*(3–4), 425–441. https://doi.org/10.1130/B31335.1

Eddy, M. P., Clark, K. P., & Polenz, M. (2017). Age and volcanic stratigraphy of the Eocene Siletzia oceanic plateau in Washington and on Vancouver Island. *Lithosphere*, *9*(4), 652–664. https://doi.org/10.1130/L650.1

England, T. D. J., & Calon, T. J. (1991). The Cowichan fold and thrust system, Vancouver Island, southwestern British Columbia. *The Geological Society of America Bulletin*, *103*(3), 336–362. https://doi.org/10.1130/0016-7606(1991)103<0336:TCFATS>2.3.CO;2

Englert, R. G., Hubbard, S., Coutts, D., & Matthews, W. A. (2018). Tectonically controlled initiation of contemporaneous deep-water channel systems along a Late Cretaceous continental margin, western British Columbia, Canada. *Sedimentology*, *65*(7), 2404–2438. https://doi.org/10.1111/sed.12472

Ernst, W. G., & Liu, J. (1998). Experimental phase-equilibrium study of Al- and Ti-contents of calcic amphibole in MORB—A semiquantitative thermobarometer. *American Mineralogist*, *83*(9–10), 952–969. https://doi.org/10.2138/am-1998-9-1004

Evans, T. P. (2004). A method for calculating effective bulk composition modification due to crystal fractionation in garnet-bearing schist: Implications for isopleth thermobarometry. *Journal of Metamorphic Geology*, *22*(6), 547–557. https://doi.org/10.1111/j.1525-1314.2004.00532.x

Fairchild, L. H., & Cowan, D. S. (1982). Structure, petrology, and tectonic history of the Leech River Complex northwest of Victoria, Vancouver Island. *Canadian Journal of Earth Sciences*, *19*(9), 1817–1835. https://doi.org/10.1139/e82-161

Fisher, D., & Byrne, T. (1987). Structural evolution of underthrusted sediments, Kodiak Islands, Alaska. *Tectonics*, *6*(6), 775–793. https://doi.org/10.1029/TC006i006p00775

Friedman, R. M., & Armstrong, R. L. (1995). Jurassic and Cretaceous geochronology of the southern coast Belt, British Columbia, 49° to 51°N. *Special Papers – Geological Society of America*, *299*, 95–139. https://doi.org/10.1130/SPE299-p95

Fuhrman, M. L., & Lindsley, D. H. (1988). Ternary-feldspar modeling and thermometry. *American Mineralogist*, *73*(3–4), 201–215.

Garver, J. I., & Davidson, C. M. (2015). Southwestern Laurentian zircons in Upper Cretaceous flysch of the Chugach-Prince William terrane in Alaska. *American Journal of Science*, *315*(6), 537–556. https://doi.org/10.2475/06.2015.02

Gehrels, G., Rusmore, M. E., Woodsworth, G., Crawford, M., Andronicos, C., Hollister, L., et al. (2009). U-Th-Pb geochronology of the Coast Mountains batholith in north-coastal British Columbia: Constraints on age and tectonic evolution. *The Geological Society of America Bulletin*, *121*(9–10), 1341–1361. https://doi.org/10.1130/B26404.1

Groome, W. G. (2000). *Magmatism and metamorphism in the Leech River Complex, Southern Vancouver Island, British Columbia, Canada: Implications for Eocene Tectonics of the Pacific Northwest* (Master's thesis). Simon Fraser University.

Groome, W. G., & Thorkelson, D. J. (2009). The three-dimensional thermo-mechanical signature of ridge subduction and slab window migration. *Tectonophysics*, *464*(1–4), 70–83. https://doi.org/10.1016/j.tecto.2008.07.003

Groome, W. G., Thorkelson, D. J., Friedman, R. M., Mortensen, J. K., Massey, N. W. D., Marshall, D. D., & Layer, P. W. (2003). Magmatic and tectonic history of the Leech River Complex, Vancouver Island, British Columbia: Evidence for ridge-trench intersection and accretion of the crescent Terrane. *Special Papers – Geological Society of America*, *371*, 327–353. https://doi.org/10.1130/0-8137-2371-X.327

Harrichhausen, N. (2021). *Fault accommodation of permanent strain in the northern Cascadia forearc* (Doctoral thesis). University of California, Santa Barbara. Retrieved from https://escholarship.org/uc/item/5h05p9fv

Harrichhausen, N., Morell, K. D., Regalla, C., Bennett, S. E., Leonard, L. J., Lynch, E. M., & Nissen, E. (2021). Paleoseismic trenching reveals Late Quaternary kinematics of the Leech River Fault: Implications for forearc strain accumulation in northern Cascadia. *Bulletin of the Seismological Society of America*, *111*(2), 1110–1138. https://doi.org/10.1785/0120200204

Hawthorne, F. C., Oberti, R., Harlow, G. E., Maresch, W. V., Martin, R. F., Schumacher, J. C., & Welch, M. D. (2012). Nomenclature of the amphibole supergroup. *American Mineralogist*, *97*(11–12), 2031–2048. https://doi.org/10.2138/am.2012.4276

Henry, D. J., Guidotti, C. V., & Thomson, J. A. (2005). The Ti-saturation surface for low-to-medium pressure metapelitic biotites: Implications for geothermometry and Ti-substitution mechanisms. *American Mineralogist*, *90*(2–3), 316–328. https://doi.org/10.2138/am.2005.1498

Holland, T. J. B., & Powell, R. (1998). An internally consistent thermodynamic data set for phases of petrological interest. *Journal of Metamorphic Geology*, *16*(3), 309–343. https://doi.org/10.1111/j.1525-1314.1998.00140.x

Holt, A. F., & Condit, C. B. (2021). Slab temperature evolution over the lifetime of a subduction zone. *Geochemistry, Geophysics, Geosystems*, *22*(6), e2020GC009476. https://doi.org/10.1029/2020GC009476

Horstwood, M. S. A., Košler, J., Gehrels, G., Jackson, S. E., McLean, N. M., Paton, C., et al. (2016). Community-derived standards for LA-ICP-MS U-(Th-)Pb geochronology – Uncertainty propagation, age interpretation and data reporting. *Geostandards and Geoanalytical Research*, *40*(3), 311–332. https://doi.org/10.1111/j.1751-908X.2016.00379.x

Housen, B., & Beck, M. E. (1999). Testing terrane transport: An inclusive approach to the Baja B.C. controversy. *Geology*, *27*(12), 1143–1146. https://doi.org/10.1130/0091-7613(1999)027<1143:TTTAIA>2.3.CO;2

Hyndman, R. D., Yorath, C. J., Clowes, R. M., & Davis, E. E. (1990). The northern Cascadia subduction zone at Vancouver Island: Seismic structure and tectonic history. *Canadian Journal of Earth Sciences*, *27*(3), 313–329. https://doi.org/10.1139/e90-030

Irving, E. (1979). Paleopoles and paleolatitudes of North America and speculations about displaced terrains. *Canadian Journal of Earth Sciences*, *16*(3), 669–694. https://doi.org/10.1139/e79-065

Leake, B. E., Woolley, A. R., Arps, C. E. S., Birch, W. D., Gilbert, M. C., Grice, J. D., et al. (1997). Nomenclature of amphiboles: Report of the subcommittee on amphiboles of the International Mineralogical Association, Commission on new minerals and mineral names. *Mineralogical Magazine*, *61*(405), 295–310. https://doi.org/10.1180/minmag.1997.061.405.13

Li, G., Liu, Y., Regalla, C., & Morell, K. D. (2018). Seismicity relocation and fault structure near the Leech River Fault Zone, southern Vancouver Island. *Journal of Geophysical Research: Solid Earth*, *123*(4), 2841–2855. https://doi.org/10.1002/2017JB015021

Locock, A. J. (2014). An Excel spreadsheet to classify chemical analyses of amphiboles following the IMA 2012 recommendations. *Computers & Geosciences*, *62*, 1–11. https://doi.org/10.1016/j.cageo.2013.09.011

Ludwig, K. R. (2003). User's manual for Isoplot 3.00, a geochronological toolkit for Microsoft Excel. *4*, 25–32.

Maruyama, S., Liou, J. G., & Suzuki, O. (1982). The peristerite gap in low-grade metamorphic rocks. *Contributions to Mineralogy and Petrology*, *81*(4), 268–276. https://doi.org/10.1007/BF00371681

Maruyama, S., Suzuki, K., & Liou, J. G. (1983). Greenschist-amphibolite transition equilibria at low pressures. *Journal of Petrology*, *24*(4), 583–604. https://doi.org/10.1093/petrology/24.4.583

Massey, N. W. D. (1986). Metchosin Igneous Complex, southern Vancouver Island: Ophiolite stratigraphy developed in an emergent island setting. *Geology*, *14*(7), 602–605. https://doi.org/10.1130/0091-7613(1986)14%3C602:MICSVI%3E2.0.CO;2

Matharu, G., Bostock, M. G., Christensen, N. I., & Tromp, J. (2014). Crustal anisotropy in a subduction zone forearc: Northern Cascadia. *Journal of Geophysical Research: Solid Earth*, *119*(9), 7058–7078. https://doi.org/10.1002/2014JB011321

Matthews, W. A., & Guest, B. (2017). A practical approach for collecting large-n detrital zircon U-Pb data sets by quadrupole LA-ICP-MS. *Geostandards and Geoanalytical Research*, *41*(2), 161–180. https://doi.org/10.1111/ggr.12146

Matthews, W. A., Guest, B., Coutts, D., Bain, H., & Hubbard, S. (2017). Detrital zircons from the Nanaimo basin, Vancouver Island, British Columbia: An independent test of Late Cretaceous to Cenozoic northward translation. *Tectonics*, *36*(5), 854–876. https://doi.org/10.1002/2017TC004531

McCrory, P. A., & Wilson, D. S. (2013). A kinematic model for the formation of the Siletz-Crescent forearc terrane by capture of coherent fragments of the Farallon and Resurrection plates. *Tectonics*, *32*(3), 718–736. https://doi.org/10.1002/tect.20045

Meneghini, F., Marroni, M., Moore, J. C., Pandolfi, L., & Rowe, C. D. (2009). The processes of underthrusting and underplating in the geologic record: Structural diversity between the Franciscan complex (California), the Kodiak complex (Alaska) and the Internal Ligurian Units (Italy). *Geological Journal*, *44*(2), 126–152. https://doi.org/10.1002/gj.1144

Morell, K. D., Regalla, C., Amos, C., Bennett, S. E., Leonard, L. J., Graham, A., et al. (2018). Holocene surface rupture history of an active forearc fault redefines seismic hazard in southwestern British Columbia, Canada. *Geophysical Research Letters*, *45*(21), 11605–11611. https://doi.org/10.1029/2018GL078711

Morell, K. D., Regalla, C., Leonard, L. J., Amos, C., & Levson, V. (2017). Quaternary rupture of a crustal Fault beneath Victoria, British Columbia, Canada. *Geological Society of America Today*, *27*(3), 4–10. https://doi.org/10.1130/GSATG291A.1

Muller, J. E. (1977a). Evolution of the Pacific Margin, Vancouver Island, and adjacent regions. *Canadian Journal of Earth Sciences*, *14*(9), 2062–2085. https://doi.org/10.1139/e77-176

Muller, J. E. (1977b). Geology of Vancouver Island, British Columbia (Open File 463). Geological Survey of Canada. https://doi.org/10.4095/129265

Muller, J. E. (1980). *Geology, Victoria, British Columbia* (Open File 701). Geological Survey of Canada. https://doi.org/10.4095/129114

Mustard, P. S. (1994). The Upper Cretaceous Nanaimo Group, Georgia Basin. In J. Monger (Ed.), *Geology and geological hazards of the Vancouver region, southwestern British Columbia*, *Geological Survey of Canada Bulletin 481* (p. 320). https://doi.org/10.4095/203244

Nelson, J., & Colpron, M. (2007). Tectonics and metallogeny of the British Columbia, Yukon, and Alaskan Cordillera, 1.8 Ga to the present. In W. D. Goodfellow (Ed.), *Mineral deposits of Canada: A synthesis of major deposit-types, district metallogeny, the evolution of geological provinces, and exploration methods* (pp. 755–791). Geological Association of Canada, Mineral Deposits Division, Special Publication No. 5.

Palin, R. M., Weller, O. M., Waters, D. J., & Dyck, B. (2016). Quantifying geological uncertainty in metamorphic phase equilibria modelling; a Monte Carlo assessment and implications for tectonic interpretations. *Geoscience Frontiers*, *7*(4), 591–607. https://doi.org/10.1016/j.gsf.2015.08.005

Paton, C., Woodhead, J. D., Hellstrom, J. C., Hergt, J. M., Greig, A., & Maas, R. (2010). Improved laser ablation U-Pb zircon geochronology through robust downhole fractionation correction. *Geochemistry, Geophysics, Geosystems*, *11*(3), Q0AA06. https://doi.org/10.1029/2009GC002618

Pavlis, T. L., & Sisson, V. B. (1995). Structural history of the Chugach metamorphic complex in the Tana River region, eastern Alaska: A record of Eocene ridge subduction. *The Geological Society of America Bulletin*, *107*(11), 1333–1355. https://doi.org/10.1130/0016-7606(1995)107%3C1333:SHOTCM%3E2.3.CO;2

Peacock, S. M. (1987). Creation and preservation of subduction-related inverted metamorphic gradients. *Journal of Geophysical Research*, *92*(B12), 12763–12781. https://doi.org/10.1029/JB092iB12p12763

Penniston-Dorland, S. C., Kohn, M. J., & Manning, C. E. (2015). The global range of subduction zone thermal structures from exhumed blueschists and eclogites: Rocks are hotter than models. *Earth and Planetary Science Letters*, *428*, 243–254. https://doi.org/10.1016/j.epsl.2015.07.031

Phillips, B. A., Kerr, A. C., Mullen, E. K., & Weis, D. (2017). Oceanic mafic magmatism in the Siletz terrane, NW North America: Fragments of an Eocene oceanic plateau? *Lithos*, *274–275*, 291–303. https://doi.org/10.1016/j.lithos.2017.01.005

Powell, R., & Holland, T. J. B. (2008). On thermobarometry. *Journal of Metamorphic Geology*, *26*(2), 155–179. https://doi.org/10.1111/j.1525-1314.2007.00756.x

Rusmore, M. E. (1982). *Structure and petrology of pre-tertiary rocks near Port Renfrew, Vancouver Island, British Columbia* (Master's thesis). University of Washington.

Rusmore, M. E., & Cowan, D. S. (1985). Jurassic–Cretaceous rock units along the southern edge of the Wrangellia terrane on Vancouver Island. *Canadian Journal of Earth Sciences*, *22*(8), 1223–1232. https://doi.org/10.1139/e85-124

Sakaguchi, A. (1996). High paleogeothermal gradient with ridge subduction beneath the Cretaceous Shimanto accretionary prism, southwest Japan. *Geology*, *24*(9), 795–798. https://doi.org/10.1130/0091-7613(1996)024%3C0795:HPGWRS%3E2.3.CO;2

Seyler, C. E., Kirkpatrick, J. D., Faber, C., Licht, A., Šilerová, D., & Regalla, C. (2022). Major element whole rock and mineral analyses and U-Pb detrital zircon analyses of schist and metabasalt mylonites from the Leech River Shear Zone, Version 1.0. *Interdisciplinary Earth Data Alliance (IEDA)*. https://doi.org/10.26022/IEDA/112312

Shekut, S., & Licht, A. (2020). Late Middle Miocene Emergence of the Olympic Peninsula Shown by Sedimentary Provenance. *Lithosphere*, 1–20. https://doi.org/10.2113/2020/7040598

Simpson, R. W., & Cox, A. (1977). Paleomagnetic evidence for tectonic rotation of the Oregon Coast Range. *Geology*, *5*(10), 585–589. https://doi.org/10.1130/0091-7613(1977)5<585:PEFTRO>2.0.CO;2

Sisson, V. B., Hollister, L. S., & Onstott, T. C. (1989). Petrologic and age constraints on the origin of a low-pressure/high-temperature metamorphic complex, southern Alaska. *Journal of Geophysical Research*, *94*(B4), 4392–4410. https://doi.org/10.1029/JB094iB04p04392

Sláma, J., Košler, J., Condon, D. J., Crowley, J. L., Gerdes, A., Hanchar, J. M., et al. (2008). Plešovice zircon — A new natural reference material for U-Pb and Hf isotopic microanalysis. *Chemical Geology*, *249*(1–2), 1–35. https://doi.org/10.1016/j.chemgeo.2007.11.005

Spear, F. S. (1981). An experimental study of hornblende stability and compositional variability in amphibolite. *American Journal of Science*, *281*(6), 697–734. https://doi.org/10.2475/ajs.281.6.697

Spear, F. S. (1995). *Metamorphic phase equilibria and pressure-temperature-time-paths* (2nd ed.). Mineralogical Society of America.

Stewart, R. J., & Page, R. J. (1974). Zeolite Facies Metamorphism of the Late Cretaceous Nanaimo Group, Vancouver Island and Gulf Islands, British Columbia. *Canadian Journal of Earth Sciences*, *11*(2), 280–284. https://doi.org/10.1139/e74-024

Syracuse, E. M., van Keken, P. E., & Abers, G. A. (2010). The global range of subduction zone thermal models. *Physics of the Earth and Planetary Interiors*, *183*(1–2), 73–90. https://doi.org/10.1016/j.pepi.2010.02.004

Tajčmanová, L., Connolly, J. A. D., & Cesare, B. (2009). A thermodynamic model for titanium and ferric iron solution in biotite. *Journal of Metamorphic Geology*, *27*(2), 153–165. https://doi.org/10.1111/j.1525-1314.2009.00812.x

Timpa, S., Gillis, K. M., & Canil, D. (2005). Accretion-related metamorphism of the Metchosin Igneous Complex, southern Vancouver Island, British Columbia. *Canadian Journal of Earth Sciences*, *42*(8), 1467–1479. https://doi.org/10.1139/e05-043

Tréhu, A. M., Asudeh, I., Brocher, T. M., Luetgert, J. H., Mooney, W. D., Nabelek, J. L., & Nakamura, Y. (1994). Crustal architecture of the Cascadia forearc. *Science*, *266*(5183), 237–243. https://doi.org/10.1126/science.266.5183.237

Ujiie, K. (2002). Evolution and kinematics of an ancient décollement zone, mélange in the Shimanto accretionary complex of Okinawa Island, Ryukyu Arc. *Journal of Structural Geology*, *24*(5), 937–952. https://doi.org/10.1016/S0191-8141(01)00103-1

Wells, R., Bukry, D., Friedman, R., Pyle, D., Duncan, R., Haeussler, P., & Wooden, J. (2014). Geologic history of Siletzia, a large igneous province in the Oregon and Washington Coast Range: Correlation to the geomagnetic polarity time scale and implications for a long-lived Yellowstone hotspot. *Geosphere*, *10*(4), 692–719. https://doi.org/10.1130/GES01018.1

Wells, R., Engebretson, D. C., Snavely, P. D., Jr., & Coe, R. S. (1984). Cenozoic plate motions and the volcano-tectonic evolution of western Oregon and Washington. *Tectonics*, *3*(2), 275–294. https://doi.org/10.1029/TC003i002p00275

Whitmeyer, S. J., & Karlstrom, K. E. (2007). Tectonic model for the Proterozoic growth of North America. *Geosphere*, *3*(4), 220–259. https://doi.org/10.1130/GES00055.1

Yorath, C. J., Sutherland Brown, A., & Massey, N. W. D. (1999). *Lithoprobe, southern Vancouver Island, British Columbia* (Open File 498). Geological Survey of Canada. https://doi.org/10.4095/210350

Zumsteg, C. L., Himmelberg, G. R., Karl, S. M., & Haeussler, P. J. (2003). Metamorphism within the Chugach accretionary complex on southern Baranof Island, southeastern Alaska. *Special Papers – Geological Society of America*, *371*, 253–267. https://doi.org/10.1130/0-8137-2371-X.253